ORIGINAL ARTICLE

Baroclinicity and directional shear explain departures from the logarithmic wind profile

Khaled Ghannam | Elie Bou-Zeid

Department of Civil and Environmental Engineering, Princeton University, Princeton, New Jersey, USA

[1]Department of Civil and Environmental Engineering, Princeton University, Princeton, New Jersey, USA

Correspondence
Khaled Ghannam, Department of Civil and Environmental Engineering, Princeton University, Princeton, New Jersey, USA 08540
Email: kghannam@princeton.edu

Funding information
Princeton Environmental Institute's Climate and Energy Grand Challenge Program and the NOAA-Princeton Cooperative Institute for Climate Science. The LES runs were performed on the supercomputers of the National Center for Atmospheric Research under project UPRI0007.

Similarity and scaling arguments underlying the existence of a logarithmic wind profile in the atmospheric surface layer (ASL) rest on the restrictive assumptions of negligible Coriolis effects (no wind turning in the ASL) and vertically uniform pressure gradients (barotropic atmospheric boundary layer (ABL)). This paper relaxes these asymptotic arguments to provide a realistic representation of the ASL where the common occurrence of baroclinicity (height-dependent pressure gradients) and wind turning, traditionally treated as outer-layer attributes, take part in modulating the ASL. The approximation of a constant-stress ASL is first replaced by a refined model for the Reynolds stress derived from the mean momentum equations to incorporate the cross-isobaric angle (directional shear) and a dimensionless baroclinicity parameter (geostrophic shear). A model for the wind profile is then obtained from first-order closure principles, correcting the log-law with an additive term that is linear in height and accounts for the combined effects of wind turning and baroclinicity. Both the stress and wind models agree well with a suite of large eddy simulations in the barotropic and baroclinic ABL. The findings provide a methodology for the extrapolation of near-surface winds to some 200 m in the near-neutral ABL for wind energy applications, the validation of the surface cross-isobaric angle in weather and climate models, and the interpretation of wind turning in field measurements and numerical experiments of the Ekman boundary layer.

KEYWORDS

Logarithmic wind profile; Rossby number similarity; Wind turning; Baroclinicity; Thermal wind

1 | INTRODUCTION

Accurate representation of the wind and momentum flux profiles above land or ocean surfaces is an increasingly pressing inquiry in a wide range of applications, including the extrapolation of near surface winds to higher elevations in the atmospheric boundary layer (ABL) (Gualtieri and Secci, 2012; Simiu et al., 2016), and the long-standing need for improved parameterization of surface boundary conditions in coupled land-atmosphere models (Floors et al., 2013; Ansorge, 2019). The latter has traditionally focused on surface drag (e.g. Wu, 1980; Garratt, 1994), but some studies have also noted the inadequate representation of the surface cross-isobaric angle (orientation of surface winds relative to the geostrophic flow aloft) in operational weather models (Brown et al., 2005), with a tendency to underestimate wind turning (Svensson and Holtslag, 2009). The fast growth in the wind energy industry has also invited considerable attention to the development of wind profile models at heights extending to 100-200 m in the ABL (Gryning et al., 2007; Draxl et al., 2014; Peña et al., 2016; Murthy and Rahi, 2017; Holtslag et al., 2017; Yang et al., 2017; Kent et al., 2018). Reliable models for the wind and wind shear at such hub heights are critical in the assessment of wind power potential for farm siting and for estimating fatigue loads on wind turbines (Calaf et al., 2010; Mirocha et al., 2018).

At the center of the foregoing discussion is the logarithmic wind profile in the atmospheric surface layer (ASL), its vertical extent, and its link to the constant stress assumption often invoked in flux-gradient closure models. While a constant stress profile is characteristic of zero pressure-gradient boundary layers, Monin and Obukhov (1954) suggested that it remains a ‘practical’ approximation in the ASL, which they estimated as a layer of $\sim$ 50 m depth above the surface where a 20% change in the stress from its surface value is tolerable for a constant stress assumption. In arriving at these estimates, Monin and Obukhov (1954) discarded the partial compensation to the pressure gradient by the Coriolis force, and further approximated that the effect of this pressure gradient results in $\sim$20% change in the stress within the ASL. The logarithmic wind profile can then be obtained from dimensional analysis or through first-order closure principles with a turbulent viscosity[1] $K_m = \kappa u_* z$, κ being the von Kàrmàn constant, u_* the friction velocity, and z the height above a surface with roughness length z_0. These scaling laws are the foundation of modern micrometeorology, and although field measurement campaigns such as the Kansas experiment did not establish a constant stress even within 20-30 m above the surface (Haugen et al., 1971; Businger et al., 1971), the discussion on any departure from the logarithmic profile was largely limited to a possible uncertainty in the von Kàrmàn constant (Tennekes, 1973; Kaimal and Wyngaard, 1990; Högström, 1996). However, in discarding the effects of the Coriolis force, this (practically constant stress) framework also has the strict requirement that the wind vector does not change direction in the ASL (wind turning is limited to the outer layer). The latter requirement gives rise to an inconsistency on whether the log-law applies for the wind speed (magnitude of the wind vector) as is commonly assumed in large

[1]It is not uncommon to reverse this argument and derive $K_m = \kappa u_* z$ as the eddy viscosity on the basis that the stress is constant ($= u_*^2$) and the wind profile is logarithmic. All these arguments however are a consequence of the assumption that κz and a unique u_* are the only length and velocity scales in the ASL.

eddy simulation (LES) and direct numerical simulation (DNS) of the Ekman boundary layer (e.g. Coleman et al., 1990; Spalart et al., 2008; Jiang et al., 2018), or for the longitudinal wind component in the direction of surface stress as understood in field measurements (e.g. tall meteorological towers), where the reference frame is aligned with the mean wind direction locally (i.e. at each height) (e.g. Carl et al., 1973; Horiguchi et al., 2012). Admittedly, the two approaches must be identical in theory, namely in the limit of an infinite surface Rossby number (Blackadar and Tennekes, 1968; Tennekes, 1973), yet the disparity is a direct consequence of the asymptotic nature of this theory.

Tennekes (1973) argued that the derivation of a logarithmic wind profile in the ASL is independent from the constant-stress assumption, and similar to its derivation in the canonical turbulent boundary layer at an infinite Reynolds number (Katul et al., 2013; Klewicki and Oberlack, 2015), the log-law results from similarity principles based on an infinite surface Rossby number $Ro = G_0/f z_0$ (f is the Coriolis parameter and G_0 is the magnitude of the surface geostrophic wind vector). It is only in this ($Ro \to \infty$) limit that the dimensionless heights z/z_0 and fz/u_* determine a similarity solution for the inner layer ($fz/u_* \to 0$ but finite z/z_0) and the outer 'Ekman' layer ($z/z_0 \to \infty$ but finite fz/u_*), respectively. An asymptotic matching of these solutions and their derivatives in an overlap (inertial) region results in a logarithmic wind profile. Nevertheless, this asymptotic matching procedure may not provide a realistic representation of ABL flows: the Ro similarity theory itself predicts the geostrophic drag coefficient u_*/G_0 and surface cross-isobaric angle α_0 as decreasing functions of Ro (e.g. Hess and Garratt, 2002; Zilitinkevich and Esau, 2005), such that α_0 becomes asymptotically zero only as $Ro \to \infty$. In practice, the ASL typically resides between the constant eddy-viscosity limit proposed by Ekman (1905) ($\alpha_0 = \pi/4$) and the infinite Ro limit of the similarity theory ($\alpha_0 \to 0$). A consequence of this finite Ro effect is that the outer layer modulates the ASL (Tennekes, 1973), i.e. an ASL where $fz/u_* \to 0$ but z/z_0 remains finite is limited to heights extremely close to the surface. This has important implications on the vertical extent of the logarithmic wind profile as the effects of directional shear due to wind turning become more pronounced near the surface, hence requiring a proper account of the cross-isobaric angle in modelling the wind and stress profiles.

In itself, the assumption that Ro is the only external parameter restricts the similarity theory to a steady-state, neutral, and barotropic ABL (mean pressure gradients or geostrophic winds do not vary with height). Among other common departures from this idealization, such as unsteadiness (e.g. Momen and Bou-Zeid, 2016; Pan and Patton, 2017; Cava et al., 2019) and/or buoyancy (e.g. Salesky et al., 2013; Ghannam et al., 2017), the effects of baroclinicity on the wind and stress profiles remain poorly studied. Baroclinicity arises from large scale horizontal temperature gradients, leading to height-dependent atmospheric pressure gradients from the thermal wind balance. These effects are difficult to disentangle in single-point field measurements (meteorological towers), and LES experiments have offered a deeper insight into their profound implications on the dynamics of the ABL (Brown, 1996; Sorbjan, 2004; Momen et al., 2018). At least from a theoretical/modelling perspective, the effects of baroclinicity on the logarithmic wind profile and its interaction with wind turning are largely unexplored. This theoretical challenge is primarily associated with the additional similarity parameters (geostrophic shear and its orientation angle) that baroclinicity introduces to the parameter space of the ABL. As a result, and since field measurements often encode a strong signature of thermal winds (Arya and Wyngaard, 1975; Floors et al., 2015), the discussion on the exact value of the von Kàrmàn constant as inferred from log-law fits to observational data becomes hardly warranted. Evidently, the tendency in interpreting field measurements is to dismiss baroclinicity as a large scale (outer layer) effect (Floors et al., 2013), and most studies have focused on its consequences on the resistance laws for u_*/G_0 and α_0 (e.g. Hess, 1973; Arya, 1978). It must be acknowledged that some studies have provided analytical solutions for the baroclinic Ekman layer with height-dependent eddy viscosity profiles (Nieuwstadt, 1983; Berger and Grisogono, 1998), but these solutions appear in the form of hypergeometric functions that are less useful in practical applications, at least compared to the ease of use of the logarithmic wind profile. The recent work by Momen et al. (2018) also proposed a closed form model for the velocity profiles throughout the baroclinic ABL using the parabolic eddy viscosity model of O'Brien (1970). While the model (consisting of two ordinary differential equations) needs to be integrated numerically using an iterative approach, its predictions matched well with the LES output for a variety of geostrophic wind profiles.

The objective of this paper is to incorporate wind turning and baroclinicity in an analytical model for the wind profile in the lowest few hundred meters of the neutral ABL. The central thesis is not so much to argue against the existence of a logarithmic scaling, albeit its theoretic character in the baroclinic ABL remains uncorroborated, but rather to emphasize that the asymptotic nature of its derivation limits its vertical extent and/or its link to a constant stress assumption in practical applications. We therefore focus first on the derivation of an improved model for the stress profile that accounts for Coriolis effects and geostrophic shear, which forms the basis for a more accurate wind profile using the traditional eddy viscosity closure. Model validation relies on a suite of LES experiments that span the barotropic ABL at different surface Rossby numbers to investigate the increased effect of wind turning in the ASL as Ro decreases, and several baroclinic cases where the magnitude and/or direction of the geostrophic wind vector are varied. The rest of the paper is organized to provide a brief background and definitions in section 2, theory and model development in section 3, LES setup in section 4, followed by results and model validation in section 5 and conclusions in section 6.

2 | EQUATIONS OF MOTION AND DEFINITIONS

This section introduces the equations of motion and provides a brief background on the main arguments of the Rossby number similarity theory. In a steady-state ABL over a flat terrain with a hydrodynamic roughness length z_0, the mean horizontal momentum equations in the Boussinesq approximation reduce to (e.g. Stull, 1988)

$$f\left(\overline{V}-V_g\right)=-\frac{\mathrm{d}\tau_x}{\mathrm{d}z}, \tag{1}$$

$$f\left(\overline{U}-U_g\right)=\frac{\mathrm{d}\tau_y}{\mathrm{d}z}, \tag{2}$$

where $(\overline{U},\overline{V})$ are the mean horizontal wind components along the (x,y) plane (parallel to the surface); ($\tau_x=-\overline{u'w'}$, $\tau_y=-\overline{v'w'}$) are the corresponding kinematic stresses; $(U_g,V_g)=(\rho f)^{-1}\left(-\frac{\partial P}{\partial y},\frac{\partial P}{\partial x}\right)$ are the geostrophic wind components that represent the horizontal gradients in mean (large-scale) pressure P, and can depend on the height (z) above the surface in baroclinic conditions; ρ is the fluid density and f is the Coriolis parameter (here for the northern hemisphere). An overbar denotes Reynolds averaging (over time and the (x,y) plane for the LES outputs); and primes indicate turbulent fluctuations around this average.

Scaling and dimensional arguments for Equations 1 and 2 have mostly relied on the assumption of a barotropic ABL where the magnitude of the geostrophic wind vector $G_0=\left[U_g(0),V_g(0)\right]$ is height-independent. The available velocity scales are then G_0 and the surface friction velocity u_* (defined by $u_*^4=\tau_{x0}^2+\tau_{y0}^2$ with subscript 0 indicating a value at the surface z_0), and the length scales are z_0 and u_*/f. Since the equations of motion do not stipulate which combination of velocity and length scales are appropriate for the problem, the choice of external (G_0 and z_0) or internal

(u_* and u_*/f) scales results in the dimensionless forms

$$\frac{1}{Ro}\frac{\overline{V}-V_g}{G_0} = -\frac{\mathrm{d}\left(\tau_x/G_0^2\right)}{\mathrm{d}\left(z/z_0\right)}; \qquad \frac{1}{Ro}\frac{\overline{U}-U_g}{G_0} = \frac{\mathrm{d}\left(\tau_y/G_0^2\right)}{\mathrm{d}\left(z/z_0\right)}, \tag{3}$$

and

$$\frac{\overline{V}-V_g}{u_*} = -\frac{\mathrm{d}\left(\tau_x/u_*^2\right)}{\mathrm{d}\left(fz/u_*\right)}; \qquad \frac{\overline{U}-U_g}{u_*} = \frac{\mathrm{d}\left(\tau_y/u_*^2\right)}{\mathrm{d}\left(fz/u_*\right)}, \tag{4}$$

respectively. The use of G_0 and z_0 in Equations 3 is intended to depict the surface Rossby number explicitly such that taking the limit $Ro \to \infty$ would result in constant stress profiles, provided that z/z_0 remains finite and $fz/u_* \to 0$. Blackadar and Tennekes (1968) presented this argument using u_* (instead of G_0) as a velocity scale so that the dimensionless number u_*/fz_0 appears instead of Ro in Equations 3, but in either case the limits $Ro \to \infty$ or $u_*/fz_0 \to \infty$ yield a definition of the ASL as an analogue to the inner (viscous) region of the canonical turbulent boundary layer (George and Castillo, 1997). The velocity defect laws in Equations 4 characterize the outer layer, namely where the normalized stresses and velocity deficits are unique functions of the dimensionless height fz/u_*, provided u_* remains the proper velocity scale for the outer layer. Consequently, the logarithmic law $\overline{U}/u_* = \kappa^{-1}\ln(z/z_0)$ is derived in the ASL by matching the slopes of the inner layer velocity profiles, $\overline{U}/u_* = \mathcal{F}(z/z_0)$ and $\overline{V}/u_* = 0$, to those of the outer layer velocity defect profiles (Equations 4) in the limit $Ro \to \infty$.

It is worth emphasizing that $\overline{V} = 0$ results from aligning the reference frame (x-axis) with the surface stress or near surface wind such that $\tau_x = u_*^2$ and $\tau_y = 0$, and hence the geostrophic wind would be oriented at an angle α_0 (cross-isobaric angle) relative to the x-axis. The alternative choice of aligning the reference frame with the surface geostrophic wind results in $\overline{V} \neq 0$, i.e. the surface wind vector is oriented at α_0 relative to the x-axis. These two choices are simply a rotation of the x-axis at the surface by an angle α_0, and in either case the $Ro \to \infty$ limit requires that α_0 remains constant throughout the ASL, namely $\overline{V}$ in the ASL must remain equal to its near-surface value (0 or constant) (Tennekes, 1973).

The angle α_0 and its relation to the geostrophic drag coefficient u_*/G_0 are also determined from the asymptotic matching procedure (e.g. Peña et al., 2010):

$$\sin(\alpha_0) = \frac{B}{\kappa}\frac{u_*}{G_0}, \tag{5}$$

where B is an empirical but supposedly universal parameter (Clarke and Hess, 1974; Arya, 1975). The universality of B is a consequence of the aforementioned matching procedure in a steady state, neutral, and barotropic ABL. However, its determination from field measurements has shown large scatter, with an average estimate of $B \approx 4.4$ (Hess and Garratt, 2002). Numerical experiments suggest $B \approx 2.7$ in LES (Andren et al., 1994), and $B \approx 2.3$ in the high Reynolds number range of the DNS experiments by Spalart et al. (2008). The elusive nature of this parameter in field measurements has been attributed to the presence of baroclinicity and heat entrainment in the atmosphere, and Zilitinkevich and Esau (2002) argued that B is a function of static stability in the free troposphere and of the ABL height (z_i). The height z_i scales with u_*/f via the Rossby-Montgomery formula (Rossby and Montgomery, 1935; Zilitinkevich, 1972)

$$c = \frac{u_*}{fz_i}, \tag{6}$$

where the parameter c typically ranges between 2 and 6 in field measurements (Hess and Garratt, 2002). Note that both B and c can depend on baroclinicity, and Arya and Wyngaard (1975) and Arya (1978) denoted z_i as a scale height rather than an ABL height in a baroclinic atmosphere.

In the baroclinic ABL, the geostrophic winds in the equations of motion become height-dependent, and Ro and u_* are no longer sufficient to describe a similarity solution akin to Equations 3 and 4. The geostrophic shear vector $(\mathrm{d}U_g/\mathrm{d}z,\ \mathrm{d}V_g/\mathrm{d}z)$ therefore has to be taken into account (Hess, 1973). These gradients can be approximated from the thermal wind equations

$$\frac{\mathrm{d}U_g}{\mathrm{d}z} \approx -\frac{g}{f\theta_r}\frac{\partial\overline{\theta}}{\partial y}, \qquad \frac{\mathrm{d}V_g}{\mathrm{d}z} \approx \frac{g}{f\theta_r}\frac{\partial\overline{\theta}}{\partial x}, \tag{7}$$

where θ_r is a reference Boussinesq temperature, g is the gravitational acceleration, and $\overline{\theta}$ is a Reynolds-averaged potential temperature. A total derivative is used in these equations for the steady state ABL and when additional terms proportional to vertical gradients in potential temperature ($\partial\overline{\theta}/\partial z$) are negligibly small compared to their horizontal counterparts (Arya and Wyngaard, 1975). When temperature gradients exist in the y-direction only, the baroclinic ABL is either under positive shear ($\mathrm{d}U_g/\mathrm{d}z > 0$) or negative shear ($\mathrm{d}U_g/\mathrm{d}z < 0$), both with $\mathrm{d}V_g/\mathrm{d}z = 0$. In these cases the geostrophic wind vector does not rotate with height and the isobars remain parallel to the isotherms (this is at times referred to as an equivalent barotropic atmosphere) (Wallace and Hobbs, 2006). Conversely, when $\mathrm{d}U_g/\mathrm{d}z = 0$, warm ($\mathrm{d}V_g/\mathrm{d}z < 0$) and cold ($\mathrm{d}V_g/\mathrm{d}z > 0$) advection arise due to temperature gradients along the isobars (Sorbjan, 2004), and the geostrophic wind vector rotates with height leading to directional geostrophic shear. The effects of baroclinicity can be generally characterized by the total geostrophic shear and its orientation angle (Arya and Wyngaard, 1975)

$$\Gamma = \sqrt{\left(\frac{\mathrm{d}U_g}{\mathrm{d}z}\right)^2 + \left(\frac{\mathrm{d}V_g}{\mathrm{d}z}\right)^2}, \qquad \beta = \tan^{-1}\left(\frac{\mathrm{d}V_g/\mathrm{d}z}{\mathrm{d}U_g/\mathrm{d}z}\right), \tag{8}$$

which can be height-dependent, but here we focus on linear variations of the geostrophic winds (constant geostrophic shear) within the ABL, such that $\Gamma = \Gamma_0$ and $\beta = \beta_0$.

In the next section, we develop a model that incorporates the aforementioned effects of wind turning (i.e. finite Ro effects leading to $\overline{V} \neq$ constant) and baroclinicity on the stress and wind profiles in the lower part of the ABL. Again, the premise is that the 'theoretical' ASL, defined as the region where $fz/u_* \to 0$ but finite z/z_0, is confined to a very thin layer (close to the surface) at finite Ro, such that the effects of the Coriolis force and baroclinicity on the wind profiles are non-negligible even in the lowest 50-100 m of the ABL. We first simplify the equations of motion to obtain a reduced expression for the Reynolds stress profile (subsection 3.1), which will require a model for the cross-isobaric angle (subsection 3.2). The wind profile is then derived in subsection 3.3.

3 | THEORY

We consider Equations 1 and 2 in a coordinate system aligned with the geostrophic wind vector at the surface such that $U_g(0) = G_0$ and $V_g(0) = 0$. The mean horizontal wind, geostrophic wind, and total stress have magnitudes $M(z) = \sqrt{\overline{U}^2 + \overline{V}^2}$, $G(z) = \sqrt{U_g^2 + V_g^2}$, and $\tau(z) = \sqrt{\tau_x^2 + \tau_y^2}$, respectively, with generally height-dependent orientation angles defined by

$$\tan(\alpha_M) = \frac{\overline{V}}{\overline{U}}; \qquad \tan(\alpha_G) = \frac{V_g}{U_g}; \qquad \tan(\alpha_\tau) = \frac{\tau_y}{\tau_x} = \frac{-\overline{v'w'}}{-\overline{u'w'}}. \tag{9}$$

These angles are defined in the interval $[-\pi, \pi]$ (full trigonometric circle) relative to the surface geostrophic wind direction ($\alpha_G(0) = 0$). In this form, the boundary conditions for the mean wind and stress components become

$$\vec{M}_0 = \begin{bmatrix} 0 \\ 0 \end{bmatrix}, \quad \text{and} \quad \vec{\tau}_0 = \begin{bmatrix} \tau_{x0} = u_*^2 \cos(\alpha_0) \\ \tau_{y0} = u_*^2 \sin(\alpha_0) \end{bmatrix}; \quad \text{at} \quad z = z_0 \tag{10}$$

and

$$\vec{M} = \begin{bmatrix} U_g \\ V_g \end{bmatrix}, \quad \text{and} \quad \vec{\tau} = 0 = \begin{bmatrix} \tau_x = 0 \\ \tau_y = 0 \end{bmatrix}; \quad \text{at} \quad z \to \infty. \tag{11}$$

where $\alpha_0 = \alpha_\tau(0) = \alpha_M(z \to z_0)$ is the angle between the surface stress (or near surface) wind and the surface geostrophic wind.

In our LES and the analyses to follow, the geostrophic wind profiles are considered to vary linearly with height; a good approximation in the ABL (Arya and Wyngaard, 1975). These profiles are

$$\frac{U_g}{G_0} = 1 + \frac{U_T}{G_0}\frac{z}{\delta}; \qquad \frac{V_g}{G_0} = \frac{V_T}{G_0}\frac{z}{\delta}, \tag{12}$$

such that the geostrophic shear components (thermal winds gradients in s^{-1}) are $\mathrm{d}U_g/\mathrm{d}z = U_T/\delta = \Gamma_0\cos(\beta_0)$ and $\mathrm{d}V_g/\mathrm{d}z = V_T/\delta = \Gamma_0\sin(\beta_0)$, where U_T and V_T are the components of the thermal wind vector at a height δ (e.g. top of the ABL) relative to the surface. In a barotropic ABL, $U_T = V_T = 0$.

3.1 | Reynolds stress profile

Using our aforementioned convention, we rewrite Equations 4 as

$$\hat{M}\sin(\alpha_M) - \hat{G}\sin(\alpha_G) = -\frac{\mathrm{d}}{\mathrm{d}\hat{z}}\left[\hat{\tau}\cos(\alpha_\tau)\right], \tag{13a}$$

$$\hat{M}\cos(\alpha_M) - \hat{G}\cos(\alpha_G) = \frac{\mathrm{d}}{\mathrm{d}\hat{z}}\left[\hat{\tau}\sin(\alpha_\tau)\right], \tag{13b}$$

where the $\hat{}$ symbol represents dimensionless variables ($\hat{M} = M/u_*$, $\hat{G} = G/u_*$, $\hat{\tau} = \tau/u_*^2$, and $\hat{z} = fz/u_*$). Since in the presence of Coriolis effects the wind angle typically lies in the range $0 < \alpha_M < \pi/2$, we divide Equation 13a by $\sin(\alpha_M)$ and Equation 13b by $\cos(\alpha_M)$, which requires that $\alpha_M \neq 0$ and $\alpha_M \neq \pi/2$, and subtract them to obtain after some algebra

$$\frac{\mathrm{d}\hat{\tau}}{\mathrm{d}\hat{z}} = \frac{1}{\cos(\alpha_M - \alpha_\tau)}\left[-\hat{G}\sin(\alpha_M - \alpha_G) - \hat{\tau}\sin(\alpha_M - \alpha_\tau)\frac{\mathrm{d}\alpha_\tau}{\mathrm{d}\hat{z}}\right], \tag{14}$$

a first-order ordinary differential equation for the magnitude of the stress in terms of the external parameters G and α_G, and the internal variables α_M and α_τ. Equation 14 is merely a restatement of the equations of motion, written in reduced form such that α_M (but not M) appears in the stress profile. In the lower part of the neutral ABL, the wind vector is closely aligned with the Reynolds stress (e.g. Geernaert, 1988; Jiang et al., 2018), i.e. $\alpha_\tau \approx \alpha_M$. Equation 14 then reduces to

$$\frac{\mathrm{d}\hat{\tau}}{\mathrm{d}\hat{z}} = -\hat{G}\sin(\alpha_M - \alpha_G), \tag{15}$$

which upon integration from the surface to some height z within the ABL results in the stress profile

$$\frac{\tau(z)}{u_*^2} = 1 - \frac{f}{u_*^2}\int_{z_0}^{z} G\sin(\alpha_M - \alpha_G)\,\mathrm{d}z', \tag{16}$$

where we used the boundary condition $\tau_0 = u_*^2$. Equation 16 is a generalized profile for the magnitude of the Reynolds stress in a barotropic ($G = G_0$) or baroclinic [$G = G(z)$] ABL; the only assumption being that the stress and wind vectors are closely aligned in a region $z \ll u_*/f$. This is a common assumption in the ASL, and implies that the wind vector and the wind-shear vector are also aligned. Close to the surface, $\mathrm{d}\overline{U}/\mathrm{d}z \sim \overline{U}/(z - z_0)$ and $\mathrm{d}\overline{V}/\mathrm{d}z \sim \overline{V}/(z - z_0)$, and since $\tau_x \sim d\overline{U}/dz$ and $\tau_y \sim d\overline{V}/dz$, then $\tau_y/\tau_x \sim \overline{V}/\overline{U}$, or $\alpha_\tau = \alpha_M$. Alternatively, the argument can also be made that Equation 15 (i.e. retaining only the term $-\hat{G}\sin(\alpha_M - \alpha_G)$ from Equation 14) reproduces the stress profile in the ASL accurately. This argument is plausible since the term containing $\hat{G}$ in Equation 14 is much larger than the second term. Figure S1 in the Supporting Information compares the right hand side (r.h.s.) of Equations 14 and 15 from our LES output (described later) in both the barotropic and baroclinic ABL, showing that these match very well in the ASL and hence Equation 15 provides a good model for the stress profile in the surface layer.

Some comments on this stress profile in the context of ABL modelling are noteworthy. A constant stress ($\tau = u_*^2$) commensurate with the zero pressure gradient boundary layer (ZPGBL) (e.g. George and Castillo, 1997; Wu and Moin, 2009) can be recovered from Equation 16 by setting $G = 0$, i.e. no geostrophic forcing or equivalently zero pressure gradient, but this represents the least realistic framework to investigate the ABL. In modelling the ABL as a half-channel flow (constant pressure gradient $-\rho^{-1}\partial P/\partial x = -fG = u_*^2/\delta$) without Coriolis effects, and using $\sin(\alpha_M - \alpha_G) = 1$, integrating Equation 16 results in a linear stress profile

$$\tau(z) = \tau_x(z) = u_*^2\left(1 - \frac{z - z_0}{\delta}\right) \qquad \text{and} \qquad \tau_y = 0 \qquad \text{in} \qquad 0 \le z \le \delta, \tag{17}$$

where δ is the channel half-width here. This profile shows that at $z - z_0 = 0.1\delta$ (typical depth for the ASL), the stress would decrease by 10% from its surface value, an underestimation of its decrease in a realistic ABL (e.g. exponential decay models by Zilitinkevich and Esau, 2005). To compare our model to the 'practically' constant stress approximation proposed by Monin and Obukhov (1954), we consider Equation 16 at some height $z = H$ in a barotropic ABL ($G = G_0$), where H represents a typical ASL height similar to Monin and Obukhov (1954). Rearranging, we obtain the change in the stress within this layer as

$$\frac{\tau(H) - u_*^2}{u_*^2} = -\frac{fG_0}{u_*^2}\int_{z_0}^{H} \sin(\alpha_M)\,\mathrm{d}z'; \qquad \alpha_M \neq 0. \tag{18}$$

This expression is similar to that obtained by Monin and Obukhov (1954), except that their estimates ignore the integral of $\sin(\alpha_M)$ (wind turning). Conversely, Equation 18 incorporates the cross-isobaric angle (directional shear) in modelling the stress profile in the barotropic ABL.

In its most general form however, Equation 16 can be used to model the stress profile in a baroclinic ASL. In the common cases where baroclinicity is well approximated by linear profiles of the geostrophic winds, this equation becomes

$$\frac{\tau(z)}{u_*^2} = 1 - \frac{f}{u_*^2}\left[G_0 \int_{z_0}^{z} \sin(\alpha_M)\, \mathrm{d}z' + \frac{U_T}{\delta}\int_{z_0}^{z} z' \sin(\alpha_M)\, \mathrm{d}z' - \frac{V_T}{\delta}\int_{z_0}^{z} z' \cos(\alpha_M)\, \mathrm{d}z'\right] \tag{19a}$$

$$= 1 - \int_0^{\hat{z}} \hat{G}_0 \sin(\alpha_M)\, \mathrm{d}\hat{z}' - \int_0^{\hat{z}} \frac{1}{f}\Gamma_0 \hat{z}' \sin(\alpha_M - \beta_0)\, \mathrm{d}\hat{z}'. \tag{19b}$$

The right hand side of Equation 19a expresses how the surface stress changes with height due to the surface pressure gradient and Earth's rotation (second term, as in barotropic), and the effects of positive ($U_T > 0$) or negative ($U_T < 0$) geostrophic shear (third term) and/or warm ($V_T < 0$) or cold ($V_T > 0$) advection (last term). Equation 19b uses the baroclinicity parameters [$(\Gamma_0 \cos\beta_0, \Gamma_0 \sin\beta_0) \equiv (U_T/\delta, V_T/\delta)$] to show that the profile of the normalized stress and subsequently that of $\sin(\alpha_M)$ are unique functions of the dimensionless parameters $\hat{G}_0$, $\hat{z}$, $f^{-1}\Gamma_0$, and β_0; in accordance with the similarity theory. It will prove useful to combine the two baroclinicity parameters into a dimensionless parameter γ as

$$\gamma = \frac{1}{f}\Gamma_0\left(\cos\beta_0 - \sin\beta_0\right), \tag{20}$$

which represents the effect of U_T/δ and V_T/δ. Given a known external geostrophic forcing $G(z)$, the stress profile (Equation 19) only requires a model for $\sin(\alpha_M)$.

3.2 | Cross-isobaric angle

In a barotropic ABL, the profile of $\sin(\alpha_M)$ must be a unique function of $\hat{z}$, and decreases from its surface value $\sin(\alpha_0)$ to zero near the ABL height, or at the scale height where the stress gradients vanish and the geostrophic balance is established (e.g. Arya and Wyngaard, 1975). A plausible model is $\sin(\alpha_M) = \sin(\alpha_0)\, e^{-c\hat{z}}$, which indicates that wind turning is strongest in the surface layer of the barotropic ABL. To accommodate the effects of baroclinicity on the profile of $\sin(\alpha_M)$, we use the similarity form of Equation 19b where the linearity of the last integral in $\hat{z}$ is suggestive of the implications of baroclinicity on $\sin(\alpha_M)$, which we then represent as

$$\sin(\alpha_M) = \sin(\alpha_0)\left[e^{-c\hat{z}} + \frac{\gamma}{\hat{G}_0}\hat{z}\right], \tag{21}$$

with γ as given by Equation 20, and the boundary condition $\sin(\alpha_0)$ is to be determined. The Rossby number similarity theory of the barotropic ABL predicts that $\sin(\alpha_0)$ is proportional to u_*/G_0 with the empirical parameter B (Equation 5), and Clarke and Hess (1974) argued that this relation remains valid in the baroclinic ABL but with B dependent on baroclinicity.

A relation for $\sin(\alpha_0)$ analogous to Equation 5 can be derived from our Equation 15, which when evaluated in the limit $\hat{z} \rightarrow \hat{z}_0$ gives

$$\begin{aligned} \sin(\alpha_0) &= \left(-\frac{\mathrm{d}\hat{\tau}}{\mathrm{d}\hat{z}}\right)\Bigg|_{\hat{z}\rightarrow\hat{z}_0} \frac{1}{\hat{G}_0} \\ &= \frac{B}{\kappa}\frac{u_*}{G_0}, \end{aligned} \tag{22}$$

where we used $\alpha_G(\hat{z} \to \hat{z}_0) = 0$ and $\alpha_M(\hat{z} \to \hat{z}_0) = \alpha_0$. Equation 22 is analogous to Equation 5 but obtained from independent arguments. The second line in Equation 22 makes this analogy with $B/\kappa = -(\mathrm{d}\hat{\tau}/\mathrm{d}\hat{z})|_{\hat{z}\to\hat{z}_0}$, elucidating the physical origin of B/κ as the stress gradient at the surface. The dependence of B on baroclinicity is also inferred from the last integral in Equation 19b, namely the additive term $f^{-1}\Gamma_0(f z_i/u_*)\sin(\alpha_0 - \beta_0)$, where we followed the integral-measure approach of Arya and Wyngaard (1975) and Arya (1978) to include the scale height $f z_i/u_*$ (rather than $f z_0/u_*$) in this dependence. The general relation for $\sin(\alpha_0)$ becomes

$$\sin(\alpha_0) = \frac{B}{\kappa}\frac{u_*}{G_0} \tag{23a}$$

$$\frac{B}{\kappa} = \frac{B_0}{\kappa} - \frac{1}{c}\frac{\Gamma_0}{f}\sin(\alpha_0 - \beta_0), \tag{23b}$$

where we used $c = u_*/f z_i$. Equation 23a maintains the form of the resistance law (Equation 5) of the similarity theory, but incorporates baroclinic effects on the parameter B (Equation 23b) as the sum of a barotropic part B_0, and deviations due to baroclinicity. This baroclinic deviation is similar to the form suggested by Arya (1978) for the convective ABL, which reads (in their notation) $m_2\kappa(z_i/u_*)\Gamma_0\sin(\beta_0 - \eta_m)$, where m_2 is the integral of the geostrophic shear over z_i, and η_m is an empirical phase angle. Our correction eliminates the need for η_m, but at the expense of being an implicit relation where $\sin(\alpha_0)$ appears on the r.h.s. of Equation 23b.

Given the knowledge of Γ_0, β_0, and u_*/G_0, Equation 23b relates the two unknown parameters B and c in a baroclinic ABL, such that the knowledge of either is sufficient. In general, both B and c depend on baroclinicity. The common parametric (or prognostic) approach would determine B (and subsequently $\sin(\alpha_0)$) from Equations 23 aided by the knowledge of the scale height ratio c (e.g. Arya and Wyngaard, 1975; Arya, 1978). This is often motivated by the relatively weak dependence of c on baroclinicity (see e.g. Zilitinkevich and Esau, 2003), such that when $(B/\kappa - B_0/\kappa)$ is plotted against $f^{-1}\Gamma_0\sin(\alpha_0 - \beta_0)$, the relation is close to linear (with a constant slope $-1/c$). Alternatively, an optimized (diagnostic) approach determines $B = \kappa G_0 \sin(\alpha_0)/u_*$ using Equation 23a along with observational or numerical simulation data, and diagnoses the dependence of c on baroclinicity from Equation 23b. These prognostic and diagnostic approaches will be discussed in further detail as part of the results in section 5.

Regardless of the approach, substituting Equation 23a in 21, the profile of $\sin(\alpha_M)$ becomes

$$\sin(\alpha_M) = \frac{B}{\kappa\hat{G}_0}\left[e^{-c\hat{z}} + \frac{\gamma}{\hat{G}_0}\hat{z}\right], \tag{24}$$

and hence the stress profile can be obtained by integrating Equation 19b using 24 to yield

$$\hat{\tau}(\hat{z}) = 1 + \frac{B}{c\kappa}\left[\left(e^{-c\hat{z}} - 1\right)\left(1 + \frac{\gamma}{c\hat{G}_0}\right)\right]\left[1 + \frac{2\gamma}{\hat{G}_0}\hat{z}\left(1 - \hat{z} + \hat{z}^2\right)\right], \tag{25a}$$

$$\approx 1 + \frac{B}{c\kappa}\left[\left(e^{-c\hat{z}} - 1\right)\left(1 + \frac{\gamma}{c\hat{G}_0}\right)\right]. \tag{25b}$$

The series expansion in the last bracket of Equation 25a results from truncating a Taylor series of an exponential function, but since this term is present only in baroclinic conditions ($\gamma \neq 0$) and remains small in the ASL ($\hat{z} \ll 1$), the stress can be modelled by Equation 25b with sufficient accuracy in the ASL. In accordance with the similarity theory, Equation 25b recovers a constant stress $\hat{\tau} = 1$ in the limit $\hat{z} \to 0$ for both barotropic and baroclinic conditions.

3.3 | Eddy viscosity and wind profiles

The wind speed (M) profile can now be derived using a first-order closure model. Starting with such a model for the individual wind components (with an eddy viscosity K_m)

$$\tau_x = -\overline{u'w'} = K_m \frac{d\overline{U}}{dz} \quad ; \quad \tau_y = -\overline{v'w'} = K_m \frac{d\overline{V}}{dz}, \tag{26}$$

we multiply the first of these Equations by $\overline{U}$ and the second by $\overline{V}$ and add them to obtain

$$\overline{U}\tau_x + \overline{V}\tau_y = \frac{1}{2} K_m \frac{d}{dz}\left(\overline{U}^2 + \overline{V}^2\right). \tag{27}$$

Using $\overline{U} = M\cos(\alpha_M)$, $\tau_x = \tau\cos(\alpha_\tau)$, and similarly for other terms, Equation 27 becomes

$$\tau\cos(\alpha_M - \alpha_\tau) = K_m \frac{dM}{dz}, \tag{28}$$

such that the assumption $\alpha_\tau \approx \alpha_M$ (consistent with the previous section) results in $\tau = K_m dM/dz$.

We use the linear eddy viscosity model $K_m = \kappa u_* z$ in the surface layer (the friction velocity u_* depends on baroclinicity), which while itself may be a consequence of a log-law and constant stress ASL, remains a justifiable model on the grounds that u_* is the near-surface turbulence velocity scale and κz is the dominant mixing length in the ASL in accordance with Townsend's attached eddy model (Townsend, 1961; Meneveau and Marusic, 2013; Ghannam et al., 2018). The wind profile can then be obtained by integrating $\tau = K_m dM/dz$ (from Equation 25b)

$$\frac{M(z)}{u_*} = \frac{1}{\kappa}\ln\left(\frac{z}{z_0}\right) + \frac{B}{\kappa^2}\left(\frac{fz}{u_*}\right) + \frac{B}{\kappa^2}\frac{u_*}{cG_0}\gamma\left(\frac{fz}{u_*}\right), \tag{29}$$

where we used $\hat{z} = fz/u_*$. This wind model reduces to the log-law only in the limit $fz/u_* \to 0$ (or $Ro \to \infty$), but incorporates outer layer effects due to wind turning (second term on the r.h.s.) and baroclinicity (third term on r.h.s.). The stress and wind models given in Equations 25b and 29 will now be tested against a suite of LES experiments of the neutral ABL with a variety of barotropic and baroclinic geostrophic forcing.

4 | LARGE EDDY SIMULATIONS

The LES code used herein solves the three-dimensional filtered momentum equations written in rotational form (Bou-Zeid et al., 2005; Kumar et al., 2006), such that the incompressible continuity equation is enforced by solving a Poisson equation for a modified pressure (turbulent kinetic energy is subtracted from the pressure). The general setup of the code follows Momen et al. (2018), but our setup does not include a capping temperature inversion. Such an ABL is typically referred to as truly-neutral, as opposed to conventionally-neutral ABL (no surface heating but a temperature inversion at the ABL top can result in downward heat flux). In the Supplementary Information, we reproduce some of the results presented hereafter for the conventionally-neutral barotropic and baroclinic ABL, showing that the presence of a capping inversion has negligible effects on our modelling results for the ASL. Even with no surface or entrainment buoyancy fluxes, a conservation equation for potential temperature is solved in our LES code with some modifications (discussed below) to account for the imposed large-scale horizontal temperature gradients that result in baroclinicity (Equation 7) (Brown, 1996; Momen et al., 2018). The filtered mass, momentum, and thermal energy conservation equations are

$$\frac{\partial \widetilde{u_i}}{\partial x_i} = 0; \tag{30}$$

$$\frac{\partial \widetilde{u_i}}{\partial t} + \widetilde{u_j}\left(\frac{\partial \widetilde{u_i}}{\partial x_j} - \frac{\partial \widetilde{u_j}}{\partial x_i}\right) = -\frac{1}{\rho}\frac{\partial \widetilde{p^*}}{\partial x_i} - \frac{\partial \tau_{ij}}{\partial x_i} + g\frac{\widetilde{\theta^*}}{\theta_r}\delta_{i3} + f\left(U_g - \widetilde{u_1}\right)\delta_{i2} - f\left(V_g - \widetilde{u_2}\right)\delta_{i1}; \tag{31}$$

$$\frac{\partial \widetilde{\theta^*}}{\partial t} + \widetilde{u_j}\frac{\partial \widetilde{\theta^*}}{\partial x_j} + \widetilde{u}\frac{\partial \Theta}{\partial x} + \widetilde{v}\frac{\partial \Theta}{\partial y} = -\frac{\partial \pi_j}{\partial x_j}, \tag{32}$$

where $x_i \equiv (x_1, x_2, x_3) \equiv (x, y, z)$ and $\widetilde{u_i} \equiv (\widetilde{u_1}, \widetilde{u_2}, \widetilde{u_3}) \equiv (\widetilde{u}, \widetilde{v}, \widetilde{w})$ are the position and resolved velocity vectors, respectively; τ_{ij} is the deviatoric part of the subgrid-scale (SGS) stress tensor; and δ_{ij} is the Kronecker delta. The tilde $\widetilde{\ }$ denotes the resolved component of the variables. In this form, the mean horizontal pressure gradients are imposed as prescribed geostrophic winds $(U_g, V_g) = (\rho f)^{-1}\left(-\frac{\partial P}{\partial y}, \frac{\partial P}{\partial x}\right)$ in the code. In Equations 31 and 32, $\widetilde{\theta^*}$ is a modified potential temperature that is derived to be horizontally periodic over the domain (needed because our horizontal numerical gradients are computed using pseudo-spectral methods). If one defines the Reynolds average potential temperature $\Theta = \overline{\theta}$ that varies in x and y in a baroclinic ABL, and its planar (x,y) average $\langle\Theta\rangle_{(x,y)}$, then $\widetilde{\theta^*} = \widetilde{\theta} + \langle\Theta\rangle_{(x,y)} - \Theta$. Physically, it represents the instantaneous potential temperature from which the mean horizontal trend is removed (see Momen et al. (2018) for full derivation). The advective terms $\widetilde{u}\partial\Theta/\partial x$ and $\widetilde{v}\partial\Theta/\partial y$ represent the horizontal heat transport associated with the baroclinic large scale temperature gradients, but both Brown (1996) and Momen et al. (2018) showed that the implications of these heat fluxes and the buoyant forces they generate on the wind profiles are negligible in the ABL with zero surface buoyancy flux.

In our LES code, spatial derivatives are discretized through second-order centred finite differences in the vertical (z) and pseudo-spectral differentiation in the horizontal (x, y) directions. Periodic boundary conditions are hence employed in the horizontal directions and time integration uses the second-order Adams-Bashforth method. The SGS stress is modelled with the Lagrangian averaged scale-dependent dynamic model (Bou-Zeid et al., 2005), while the SGS heat flux model uses the dynamically-computed SGS viscosity and a constant SGS Prandtl number of 0.4. The wall model computes the surface stress from the resolved horizontal velocity field at the very first grid point by assuming a local logarithmic law, with test filtering at scale 2Δ to better reproduce the mean surface stress (Bou-Zeid et al., 2005), $\Delta = \sqrt{\mathrm{d}x\mathrm{d}y}$ being the LES filter width and $\mathrm{d}x = \mathrm{d}y$ the horizontal grid spacing. Both the upper and lower boundaries are impermeable (zero vertical velocity). Furthermore, the upper boundary condition is stress-free, and both the lower and upper boundaries have zero heat flux. Since we do not have a temperature inversion, no damping or sponge layer are imposed. Including an inversion with a sponge layer has no bearing on our conclusions (see the Supplementary Information for the results with an inversion-topped ABL where a sponge layer is imposed for the upper 25% of the LES domain).

4.1 | Simulation setup and control parameters

Eleven simulations are performed here, with five barotropic cases at different surface Rossby numbers $Ro = G_0/f z_0$; one simulation without Coriolis forcing (hereafter referred to as No-Coriolis case); and five baroclinic cases where the geostrophic wind profiles are varied with height. The No-Coriolis case is a pressure-driven half-channel flow and will be used only as a benchmark for the barotropic ABL, i.e. it can be thought of as an $f \to 0$ (or $Ro \to \infty$) limit. In all these simulations, a surface roughness length $z_0 = 0.1$ m is imposed. While our barotropic cases are similar in concept to the recent work of Jiang et al. (2018), here we obtain different Ro by changing either G_0 or f, but not z_0 since this has additional implications on the effective Reynolds number in LES. The filtered equations are solved in a domain with height L_z =1500 m and dimensions $(L_x, L_y, L_z) = (2\pi, 2\pi, 1) \times L_z$. The baroclinic pressure gradients vary linearly with height only up to $\delta = 1000$ m, and become constant in the top 500 m of the LES domain. This mimics baroclinicity generated by surface temperature gradients resulting in thermal winds within the ABL that then weaken aloft. The height δ and the magnitude of the surface geostrophic wind, $G_0 = \sqrt{U_g(0)^2 + V_g(0)^2} = U_g(0)$, are used as the characteristic length and velocity scales to solve the filtered equations in dimensionless form. The condition $V_g(0) = 0$ hence aligns the coordinate system with the surface geostrophic wind as per our earlier discussion in section 3. The velocity field is initialized with the geostrophic wind profiles, $\widetilde{u} = U_g$ and $\widetilde{v} = V_g$, with an additive noise sampled from a uniform distribution to randomize the initial conditions. Since the characteristic timescale (response time of the mean flow) of the ABL is the inertial oscillation period $T_i = 2\pi/f$ $[O(12\,\mathrm{h})]$ (Tennekes et al., 1972; Momen and Bou-Zeid, 2016), the simulations were first integrated on a $64 \times 64 \times 64$ numerical grid for $6T_i$ to efficiently develop the mean flow. The output was then interpolated into a finer turbulence-resolving $192\times 192 \times 256$ grid and integrated for an another $0.5T_i$ warm-up period to develop the smallest scale eddies, and then over an additional T_i for computing the flow statistics. All vertical profiles presented after this section are obtained from the high resolution grid and averaged over the last inertial period T_i.

Since we use LES to compare our proposed model (developed independently) to the logarithmic law in an Ekman boundary layer, assessing the performance of the LES code in the context of the log-layer "mismatch" or "overshoot" (Mason and Thomson, 1992) is necessary. Even in channel flows where the log-law is known to be robust (e.g. Marusic et al., 2013), a persistent problem in LES is that the simulated mean velocity may deviate from the log-law very close to the surface for reasons that include the grid resolution (or equivalently the viscosity of the SGS model), the grid aspect ratio, and/or the mismatch between the formulations of wall and SGS models. Other aspects may also be important and the issue is an active research topic and has been addressed by several studies using different SGS formulations (e.g. Bou-Zeid et al., 2005; Stoll and Porté-Agel, 2006; Brasseur and Wei, 2010; Kawai and Larsson, 2012). The code we use here has been validated for a variety of surface boundary conditions in channel flows (No-Coriolis cases), and showed improved performance in reproducing the logarithmic profile due to the dynamic and scale-dependent SGS model formulations (e.g. Bou-Zeid et al., 2005; Kumar et al., 2006). In this respect, Figure 1 shows log-law fits to the normalized mean velocity M/u_* for the No-Coriolis case (i.e. $M = \overline{U}$) at two different grid resolutions (both with L_z =1500 m), namely $64 \times 64 \times 96$ (dz =15.6 m), and $192 \times 192 \times 256$ (dz =5.8 m). The profiles of M/u_* for these resolutions collapse in the approximate range $0.01 < z/L_z < 0.1$ (Figure 1a), and the log-law fits roughly span this decade of scales. The derived value from the fits is $\kappa = 0.387$ when $z_0 = 0.1$ m is imposed (to match LES values). Note that while our wall model uses a value of $\kappa = 0.4$, this only affects the surface stress and its relation to the velocity at the first grid node, and does not constrain the value the code yields aloft. In the following sections, we will use the derived values $\kappa = 0.387$ and $z_0 = 0.1$ m to compare the log-law to the velocity profiles in the Ekman boundary layer where Coriolis effects are included.

Figure 2 shows the imposed geostrophic wind profiles (U_g and V_g) normalized by the surface value G_0. Relative to the barotropic simulations (Figure 2a), baroclinicity is imposed by varying either U_g (Figure 2b and 2c), V_g (Figure 2d and 2e), or both (Figure 2f), leading to a variety of thermal wind effects. The positive (S^+; Figure 2b) and negative (S^-; Figure 2c) shear ABL correspond to $dU_g/dz = U_T/\delta > 0$ and $dU_g/dz = U_T/\delta < 0$, respectively. Although in both cases the geostrophic wind vector $G(z)$ does not rotate with height ($V_g = 0$ and $\alpha_G = 0$ throughout the ABL), the geostrophic shear angle (cf. Equation 8) is $\beta_0 = 0$ in S^+ and $\beta_0 = 180°$ in S^-. Conversely, cases of cold (A^-; Figure 2d) and warm (A^+; Figure 2e) advection result from $dV_g/dz = V_T/\delta > 0$ and $dV_g/dz = V_T/\delta < 0$, respectively, where the angle α_G changes with height. In the mixed advection ABL (S^-A^-; Figure 2f), both U_g and V_g change with height and the profile of α_G is nonlinear in z. Note that in these simulations, $\delta = 1000$ m is fixed and U_T and V_T are varied such that the magnitude of the geostrophic shear vector Γ_0 (Equation 8) is the same for all cases. Also, at $z/\delta \geq 1$, U_g and V_g become constant (Figure 2), which allows the velocity profiles to approach their geostrophic counterparts. Since shear production is maintained in the ABL as long as dU_g/dz and dV_g/dz are nonzero, the velocity profiles may not become geostrophic within the LES domain especially that there is no temperature inversion present in our simulations (but see the Supplementary Information for inversion-topped cases). Table 1 summarizes the imposed and derived parameters for the five barotropic simulations, denoted by $B1$ to $B5$ in increasing value of Ro, while Table 2 details those for the baroclinic cases.

5 | RESULTS AND DISCUSSION

In this section we first present results from the LES output, namely the derived boundary conditions and averaged profiles for the barotropic and baroclinic ABL, followed by an evaluation of the proposed new model in section 3.

5.1 | LES results

5.1.1 | Surface boundary conditions

The Rossby number values imposed here for the barotropic ABL (Table 1) are comparable to those estimated by Hess and Garratt (2002) for atmospheric measurements, but the derived surface angle α_0 (last column in Table 1) is smaller than the measurements by roughly 5°-10°. This angle is computed from the surface stress components as $\tan^{-1}[(-\tau_{23})/(-\tau_{13})]$ in accordance with the definition in Equation 9, and compares well with the DNS results of Coleman (1999) [reported in the original work as a function of Reynolds number and reproduced by Hess and Garratt (2002) and Zilitinkevich and Esau (2002)]. It should be noted that the LES wall model, by construction, aligns the surface stress with the wind at the first grid point, yielding $\alpha_0 = \alpha_\tau(0) = \alpha_M(z \to z_0)$. The range of Ro in Table 1 is obtained by changing the Coriolis parameter f (except case $B1$ where G_0 is changed instead), leading to a narrow Ro range compared to an ABL where G_0 can be larger than the 6 m s^{-1} used here. Consequently, the range of α_0 is also limited to 15°-18°, but this angle is a decreasing function of Ro as predicted by the similarity theory. The LES-computed values (Equation 9) and the theoretical similarity predictions (Equation 22) are compared in Figure 3a, where $\sin(\alpha_0)$ is plotted against u_*/G_0 for the five barotropic cases. The linear fit (cf. Equation 22) results in a value $B = B_0 = 2.5$ (using $\kappa = 0.387$), very close to the LES values of Andren et al. (1994) and DNS of Spalart et al. (2008), but slightly smaller than the average value $B \approx 4$ reported in field measurements (Hess and Garratt, 2002). This disparity may be associated with stratification effects in the free atmosphere, unsteadiness, and/or baroclinicity that are commonly present in measurements (Zilitinkevich and Esau, 2002). Besides α_0, the height u_*/f (listed in Table 1) also shows a consistent increasing trend with Ro, i.e. the scale height $z_i = u_*/fc$ (Equation 6) is an increasing function of Ro. This is evident in the stress profiles in Figure 4c, where $\tau(z)$ approaches zero at lower heights as Ro decreases. Overall, our results suggest robust values (independent of Ro) of $B = 2.5$ and $c = 3.5$ for the neutral barotropic ABL (values for each simulation are given in Table 1), where z_i is estimated as the height at which $\tau(z)$ decreases to 5% of u_*^2 and then used to determine c from Equation 6.

Table 2 provides the parameters for the baroclinic ABL. The external parameters for these simulations are identical to those of the barotropic ABL (simulation $B2$ in Table 1), namely $G_0 = 6$ m s^{-1}, $z_0 = 0.1$ m, and $f = 1.4 \times 10^{-4}$ s^{-1}, but additionally a constant geostrophic shear $\Gamma_0 = 6 \times 10^{-3}$ s^{-1} is imposed in the form of thermal winds $(U_T/\delta, V_T/\delta)$ with different angles β_0 (given in Table 2). In these baroclinic ABLs, the parameters B and c can be functions of the parameters Γ_0 and/or β_0. Table 2 lists the diagnostic values of B obtained from the LES output, denoted B^{diag} and computed as $B/\kappa = G_0 \sin(\alpha_0)/u_*$ as per Equation 23a. These values of B and their dependence on β_0 follow the numerical model values of Arya and Wyngaard (1975) (their Figure 9) closely, with negative values of B when $\beta_0 < 0$ and small values $B = 0.5$ when $\beta = 0$ (e.g. the warm advection (A^+) and positive shear (S^+) ABLs in Table 2). To diagnose the dependence of c on baroclinicity, Figure 3b shows Equation 23b, namely the deviation of B/κ (B^{diag} as determined from LES) from its barotropic counterpart B_0/κ, plotted against $f^{-1}\Gamma_0 \sin(\alpha_0 - \beta_0)$, with all parameters obtained from the LES output. Note that the ratio of these quantities is c (see Equation 23b). While the relation in Equation 23b is theoretically nonlinear, the dependence of c on baroclinicity appears to be weak (at least for the range of simulations we conduct here), such that a linear fit (solid black line in Figure 3b) approximates this relation well (see also Zilitinkevich and Esau, 2003). This fit has a slope $-1/c$ and results in an average value of $c = 2.7$ (close to the barotropic value 3.5). The individual values of c obtained for each simulation (again via Equation 23b) are listed in Table 2 (ranging between 2.2 and 3.5).

Henceforth, we will denote our models for the cross-isobaric angle (Equation 24), shear stress (Equation 25), and wind profile (Equation 29) as diagnostic when the values of B^{diag} as obtained from LES (and used to infer c using Equation 23b) are used. In addition, based on the observation that the the fitted value $c = 2.7$ gives a good measure of the scale height ratio of the baroclinic ABL, one can use this average value to obtain the prognostic values of B using Equation 23b. This gives B^{prog} in Table 2, showing that these remain very close to their diagnostic counterpart. When $c = 2.7$ and B^{prog} are used, the model is referred to as prognostic since it can be applied without the need for any LES results (within the parameter space we investigate in this paper).

5.1.2 | LES profiles

While half-channel flows are often used as a model of the barotropic ABL, the stress in the ABL drops much faster than the linear decrease of the half-channel (No-Coriolis case in Figure 4c), particularly as Ro becomes smaller. This analogy hence leads to a substantial overestimation of the ABL height (e.g. the height at which the stress reduces to 5% of u_*^2). The nonlinear decrease in the stress profile within the ABL (Figure 4c), which we modelled as an exponential in section 3 (Equation 25), also indicates that the departure from a constant stress approximation (say 20% drop from its surface value) occurs much closer to the surface than is typical in channel flows. As the difference between the barotropic ABL and a channel flow is merely due to the presence of Coriolis effects here, we turn to the profile of the cross-isobaric angle α_M shown in Figure 4b. These profiles closely follow their stress counterparts in Figure 4c as to Ro effects, therefore elucidating the important role of the Coriolis force and subsequently directional shear (wind turning) in shaping the stress profiles. In Figure 4b we also point to the fact that α_M in the barotropic ABL resides between the constant eddy-viscosity solution provided by Ekman (1905) (shown as dashed line) and the $Ro \to \infty$ limit of the similarity theory (No-Coriolis case), and that wind turning becomes more pronounced in the ASL at lower Ro.

In essence, all these characteristics result from Ro effects on the ABL height, namely that smaller Ro (or smaller ABL height) lead to stronger interactions between the inner and outer layers. When plotted against fz/u_* (instead of z in Figure 4), the profiles of τ/u_*^2 and/or $\sin(\alpha_M)/\sin(\alpha_0)$ at different Ro collapse onto a universal profile (as we illustrate and discuss later in Figure 6).

Figure 4d shows the difference between the stress and wind vector directions in the barotropic ABL. As Ro increases, $\alpha_\tau - \alpha_M$ becomes smaller and the assumption on the alignment of the stress and wind vectors is plausible for a more extensive vertical range (Figure 4d). Nevertheless, while the difference $\alpha_\tau - \alpha_M$ can be $\approx -35°$ at low Ro within the lowest 200 m of the ABL, this misalignment has minor effects on our modelling arguments for the barotropic ABL. In reducing Equation 14 to Equation 15, we noted that the first term on the r.h.s. includes G/u_* and is much larger than the second term (see also Figure S1 in Supplementary Information). The collapse of the normalized wind profiles shown in Figure 4a suggests that u_* is the proper velocity scale in the lower part of the barotropic ABL. The logarithmic law (also shown in Figure 4a) remains limited to 20-30 m above the surface for the ABL with rotation, but more extensive for the No-Coriolis case (see inset in Figure 4).

In Figure 5a and 5b, the profiles of the wind and its orientation angle relative to the geostrophic wind vector exhibit profound differences between the baroclinic ABL and its barotropic counterpart. The surface friction velocity u_* no longer collapses the wind profiles (as opposed to Figure 4a) since the varying pressure gradients introduce height-dependent shear in the ASL in addition to the surface stress. More importantly, these wind profiles also do not follow the log-law (Figure 5a and its inset). Above the ASL, the wind decreases towards its geostrophic counterpart in the negative shear (S^-) and mixed-advection (S^-A^-) ABL as U_g decreases with height in these cases. This reduction in the wind is associated with strong directional shear in the middle of the ABL as depicted by the stress profiles in Figure 5c.

5.2 | Modelling the stress profile in the barotropic and baroclinic ABL

Figures 6a and 6b show the normalized profiles of the cross-isobaric angle and Reynolds stress in the barotropic ABL at different Ro. Note that $\gamma = 0$ in this barotropic ABL and hence both $\sin(\alpha_M)$ and $\tau(z)$ decrease exponentially (cf. Equations 24 and 25). These profiles are plotted against the dimensionless height fz/u_* and collapse into one line (their exponential models), indicating that u_*/f is the similarity length scale for the whole ABL, as opposed to the arguments of the similarity theory ($Ro \to \infty$) where u_*/f is regarded as an outer layer length scale only. Again, this collapse with u_*/f throughout the ABL is a consequence of finite Ro. The constants $B = 2.5$ (as obtained from Figure 3a), $c = 3.5$, and $\kappa = 0.387$ are used in Figure 6a and 6b. While an exponentially decreasing stress profile in the barotropic ABL is not a novelty in its own right, as it was also suggested by Zilitinkevich (1989) in the form $\tau(z)/u_*^2 = e^{-cfz/u_*}$ based on the similarity of the equations of motion when a constant eddy viscosity closure is employed, the explanation for this exponential behaviour and its striking connection to the profile of $\sin(\alpha_M)$ is original, and depicts the importance of wind turning (directional shear) in introducing nonlinear effects on the stress profile (compared to a channel flow). Such nonlinear effects were also typically accommodated by the form $\tau(z)/u_*^2 = (1 - z/\delta)^m$, with $m = 1/2$ or $3/4$ and δ the ABL height (e.g. Stull, 1988), but both this form and the exponential model essentially incorporate outer layer wind turning effects on the stress profile in the ASL. In addition, we note that our model in Equation 25 (with $\gamma = 0$) is identical to that of Zilitinkevich (1989) when $B/c\kappa = 1$ (here this value is 1.7). Figure 6c, 6d, and 6e show three individual examples of the performance of the stress model at different Ro (simulations $B1$, $B3$, and $B5$ in Table 1) plotted against the height z, and indicate that our assumption on the alignment of the wind and stress vectors, although not very exact, has limited implications on our model performance in the barotropic ASL.

Figure 7 shows the profiles of $\sin(\alpha_M)$ for the baroclinic ABL along with the model in Equation 24, both in its diagnostic (using c for each individual run and B^{diag}) from Table 2) and prognostic (using the average c = 2.7 and B^{prog} from Table 2) forms. The barotropic simulation $B2$, for which we use the fixed values B_0 = 2.5 and c = 3.5 (i.e. always prognostic), is reproduced in Figure 7a for reference. Both the prognostic and diagnostic forms of the model given in Equation 24 generally capture the turning of the wind with height for most baroclinic ABLs, but show some deviations (from each other and from the LES output) in the outer layer for cases A^-, A^+, and S^-A^- (Figure 7). In the lowest 250 m of these ABLs, which is the primary focus here, the diagnostic model reproduces the LES output very well. The prognostic model has slight deviations, but it may be noted that the height variation of $\sin(\alpha_M)$ is minimal in these cases (lower panel of Figure 7). While this indicates that the wind vector does not turn appreciably, the geostrophic wind vector has a height-dependent α_G in these cases and hence a cross-isobaric flow is present.

The performance of the stress model (Equation 25), in its diagnostic (dashed blue lines) and prognostic (solid black lines) versions, is depicted in Figure 8 for the baroclinic ABL. Note that Equation 25a is used to model the profiles throughout the ABL, although in the ASL Equation 25b is equally valid. In the positive shear (S^+) and warm advection (A^+) ABL, shown in Figure 8b and 8e respectively, our assumption on wind-stress alignment is acceptable even far above the surface; both of these cases exhibit a strong shear in the direction of $\overline{U}$, either due to U_g increasing with z while $V_g = 0$ (S^+), or due to constant U_g but V_g decreasing with z (A^+). Hence, Equation 25a (in its diagnostic form) accurately represents the stress profile in these cases throughout the ABL. A peculiar feature of the warm advection ABL is that the stress increases with height (Figure 8e), and in the positive shear ABL it remains approximately constant up to 500 m above the surface. In the other baroclinic ABLs, where either U_g decreases with height (S^- and S^-A^-), and/or V_g increases (A^- and S^-A^-), a distinctive layer where the stress decays from its surface value according to Equation 25 is evident in Figure 8c, 8d, and 8f for simulations S^-, A^-, and S^-A^-, respectively. Above this layer, the diagnostic model departs from the simulated profiles for these cases, but captures the inflections in the stress associated with the decrease in $\overline{U}$ (namely as τ_x changes sign to become positive in the upper part of the ABL). Evidently, this model overestimates the heights at which the inflection points occur, especially in the negative shear ABL (Figure 8c) where this inflection point is very close to the surface (roughly 50 m). Compared to its diagnostic formulation, the prognostic model performs reasonably well across all simulations (solid black lines in Figure 8). This is due to the fact that the ratio B/c appears in the stress model as a scaling factor (see Equation 25), and since these parameters are inversely related in Equation 23b, the model is less sensitive to their ratio than to the change in their individual values. Again, the weak dependence of c on baroclinicity (individual values are very close to the fitted value c = 2.7) results in very comparable values for B^{diag} and B^{prog} (Table 2), suggesting some universal, yet empirical dependence of B on the geostrophic shear angle β_0 and the scale height ratio as noted by Arya and Wyngaard (1975) and Arya (1978).

5.3 | Modelling the wind profile in the barotropic and baroclinic ABL

A comparison between the logarithmic law and the new wind profile model given in Equation 29 is shown in Figure 9 for the barotropic ABL. When plotted in outer layer coordinates, the velocity-defect $(M - G_0)/u_*$ portrays a decent collapse among different Ro values (Figure 9a). While the logarithmic profile is limited to approximately $0.03fz/u_*$, the new model proposed here matches the LES output up to $0.1fz/u_*$. In this barotropic ABL, the wind profile in Equation 29 has a linear correction $B/\kappa^2(fz/u_*)$. Apart from an additional constant, Fiedler and Panofsky (1972) arrived at a markedly similar model to Equation 29 (with $\gamma = 0$) using the nonlinear mixing length proposed by Blackadar et al. (1969). Figure 9b, 9c, and 9d illustrate examples of the wind profile M/u_* in the lowest 500 m of the ABL for simulations $B1$, $B3$, and $B5$ (increasing Ro), respectively. These show that the wind model (solid black line) matches the LES profiles up to few hundreds of meters above the surface, while the log law (grey line) is limited to few tens of meters. We emphasize that we did not refit the logarithmic profile here for each simulation (neither did we refit the parameters of our new model); for the logarithmic profile we use the values $\kappa = 0.387$ and $z_0 = 0.1$ m obtained from fitting a log-law to the velocity profile in the channel flow as discussed earlier. Hence, with $B \approx 2.5$ being a good estimate in a barotropic ABL (where $\gamma = 0$), the wind model in Equation 29 can be easily used instead of the classic log-law.

Perhaps more notably, the wind model (diagnostic and prognostic) also matches the LES profiles in the lower part of the baroclinic ABL remarkably well, as depicted in Figure 10. The vertical extent of the logarithmic profile is extremely limited in the negative shear, cold advection, and mixed-advection simulations (Figure 10c, 10d, and 10f), in large part due to the sharp decrease in the stress profiles in these cases (cf. Figure 8), such that the ASL departs from a constant stress approximation very close to the surface. Conversely, the positive shear and warm advection ABL have a more extensive logarithmic profile ($\sim$ 60 m) associated with their roughly constant stress. Nevertheless, the wind model provided by Equation 29 accurately describes the LES profiles up to few hundreds of meters, with a remarkable match up to 500 m in simulations S^+ and A^+ (Figure 10b and 10e). The model also captures the decrease (inflection point) of the wind in cases S^- and S^-A^- (Figure 10c and 10f). Minor sensitivity to the prognostic (solid line) versus diagnostic (dashed line) parameters of the wind model is noticeable above $\sim$ 100 m (Figure 10). Note that this sensitivity increases linearly with the dimensionless height fz/u_* (see Equation 29). Nevertheless, the wind model provides an accurate representation of near surface winds up to some 150-200 m above the surface even in its prognostic formulation.

Using the wind angle and wind speed models (Equations 24 and 29 with the diagnostic values of B and c), Figure 11 shows our Ekman spiral solution ($\overline{V}/G_0$ vs. $\overline{U}/G_0$) compared to the LES output. The model captures the spiral in at least the lowest 200 m of the ABL (this height is denoted by solid (blue) diamond symbols in Figure 11). This new framework thus bridges the gap between the logarithmic wind profile, valid very close to the surface in the limit $fz/u_* \to 0$, and the constant eddy-viscosity Ekman solution for the outer layer ($z/z_0 \to \infty$). It is also notable that our model exhibits excellent agreement with the LES wind spiral in the negative shear and mixed advection ABL (S^- and S^-A^-), although the stress model departed from its LES counterpart at heights $\sim$50 m in S^- and $\sim$100 m in S^-A^-. This is a consequence of the fact that the wind profile is the integral of $\tau(z)/K_m$ (this ratio is the vertical gradient of the mean velocity, which decreases with height since $K_m \propto z$), and hence the wind model becomes more robust than that of the stress (insofar the trend and inflection points in the stress are captured by its model).

6 | CONCLUDING REMARKS

The existence of a logarithmic wind and constant stress profiles in the ASL requires the very limiting assumptions of a barotropic atmosphere and negligible wind turning ($Ro \to \infty$). For a more realistic representation of the ASL, we propose a new theoretical framework that relaxes these constraints. On the assumption that the direction of the stress and wind vectors in the lower part of the neutral ABL are reasonably aligned, we first provide a model for the stress profile that incorporates the height-dependent cross-isobaric angle (due to finite Ro effects) and geostrophic wind vector (due to baroclinicity). The vertical variation of this geostrophic velocity is treated as an external (known) linear forcing, such that the magnitude of the geostrophic shear vector Γ_0 and its orientation angle β_0 suffice to describe baroclinicity. Subsequently, we exploit the arguments of the Rossby number similarity theory to model the profile of the cross-isobaric angle and derive a closed-form expression for the stress. The vertical distribution of the wind is then obtained through the traditional (linear eddy viscosity) closure.

The three main results of the work here are

$$\frac{\mathrm{d}\tau}{\mathrm{d}z} = -fG(z)\sin\left(\alpha_M - \alpha_G\right),$$

$$\frac{B}{\kappa} = \frac{B_0}{\kappa} - \frac{1}{c}\frac{\Gamma_0}{f}\sin\left(\alpha_0 - \beta_0\right),$$

$$\frac{M(z)}{u_*} = \frac{1}{\kappa}\ln\left(\frac{z}{z_0}\right) + \frac{B}{\kappa^2}\left(\frac{fz}{u_*}\right) + \frac{B}{\kappa^2}\frac{u_*}{cG_0}\gamma\left(\frac{fz}{u_*}\right),$$

The first of these provides the stress gradient in the ASL of a barotropic or baroclinic ABL (the profile of $\tau(z)$ is given in Equation 25b). This was derived on the condition that $\sin(\alpha_M - \alpha_G) \neq 0$, i.e. a cross-isobaric flow exists within the ASL at finite Ro. The second result extends the traditional resistance law (relation between surface cross-isobaric angle and geostrophic drag coefficient) to the baroclinic ABL by incorporating the dependence of the parameter B on Γ_0 and β_0. This dependence on baroclinicity remains far from trivial as it also incorporates the scale height ratio $c = u_*/fz_i$, and while this aspect of the similarity theory warrants further consideration, our findings suggest that c exhibits much weaker dependence on baroclinicity. Such a relation is useful for the validation of the surface cross-isobaric angle in weather and climate models (Brown et al., 2005; Svensson and Holtslag, 2009). The third result offers an accurate means to extrapolate near-surface winds up to some 200 m or more above land or ocean surfaces for wind energy or similar applications. It provides a correction to the log-law for wind turning (second term on right hand side) and baroclinicity (last term).

Given our models for the cross-isobaric angle and wind speed (Equations 24 and 29), we were also able to accurately predict the Ekman spiral in the lowest 200 m of the ABL, hence bridging the well-known gap between surface layer theory (log-law valid in the limit $fz/u_* \to 0$) and outer layer Ekman-type solutions ($z/z_0 \to \infty$). While we find that the empirical parameter $c \approx 3$ (from which the value of the related parameter B can be derived) may be adequate for both the barotropic and baroclinic ABL, this wind profile still requires knowledge of Γ_0 and β_0 (through γ). At a minimum, the present results serve to explain the origins of deviations from the log-law in the ASL of the commonly-occurring baroclinic ABL, even if detailed information on the baroclinicity parameters is not available.

Our results were tested against a suite of LES experiments for several barotropic ABL flows at different Ro, and several baroclinic ABL simulations where the orientation of the geostrophic wind vector is changed. We find that the logarithmic wind profile has a limited extent and a constant stress is virtually non-existent. Conversely, the provided models match the LES output within the ASL. To this end, the incorporation of wind turning and baroclinic effects provides a new approach to the interpretation of field measurements on tall (say $>$ 30 m) meteorological towers. As opposed to the approach of aligning the coordinate system locally (i.e. at each height) with the prevailing wind direction and hence masking any effects of directional shear, the profiles of the cross-isobaric angle and stress given in Equations 24 and 25 offer an alternative and more accurate approach to compute surface stresses and improve flux-gradient closure models. This approach can potentially provide information on the baroclinicity of the mesoscale environment, even if only measurements from one tower are available.

references

Andren, A., Brown, A. R., Mason, P. J., Graf, J., Schumann, U., Moeng, C.-H. and Nieuwstadt, F. T. (1994) Large-eddy simulation of a neutrally stratified boundary layer: A comparison of four computer codes. *Quarterly Journal of the Royal Meteorological Society*, **120**, 1457–1484.

Ansorge, C. (2019) Scale dependence of atmosphere–surface coupling through similarity theory. *Boundary-Layer Meteorology*, **170**, 1–27.

Arya, S. (1975) Geostrophic drag and heat transfer relations for the atmospheric boundary layer. *Quarterly Journal of the Royal Meteorological Society*, **101**, 147–161.

— (1978) Comparative effects of stability, baroclinity and the scale-height ratio on drag laws for the atmospheric boundary layer. *Journal of the Atmospheric Sciences*, **35**, 40–46.

Arya, S. and Wyngaard, J. (1975) Effect of baroclinicity on wind profiles and the geostrophic drag law for the convective planetary boundary layer. *Journal of the Atmospheric Sciences*, **32**, 767–778.

Berger, B. W. and Grisogono, B. (1998) The baroclinic, variable eddy viscosity ekman layer. *Boundary-Layer Meteorology*, **87**, 363–380.

Blackadar, A. K., Chaplin, A., Dutton, J. and Panofsky, H. (1969) Investigation of the turbulent wind field below 150-meter altitude at the eastern test range. *NASA Contractor Report*, 47–67.

Blackadar, A. K. and Tennekes, H. (1968) Asymptotic similarity in neutral barotropic planetary boundary layers. *Journal of the Atmospheric Sciences*, **25**, 1015–1020.

Bou-Zeid, E., Meneveau, C. and Parlange, M. (2005) A scale-dependent lagrangian dynamic model for large eddy simulation of complex turbulent flows. *Physics of fluids*, **17**, 025105.

Brasseur, J. G. and Wei, T. (2010) Designing large-eddy simulation of the turbulent boundary layer to capture law-of-the-wall scaling. *Physics of Fluids*, **22**, 021303.

Brown, A. (1996) Large-eddy simulation and parametrization of the baroclinic boundary-layer. *Quarterly Journal of the Royal Meteorological Society*, **122**, 1779–1798.

Brown, A., Beljaars, A., Hersbach, H., Hollingsworth, A., Miller, M. and Vasiljevic, D. (2005) Wind turning across the marine atmospheric boundary layer. *Quarterly Journal of the Royal Meteorological Society: A journal of the atmospheric sciences, applied meteorology and physical oceanography*, **131**, 1233–1250.

Businger, J. A., Wyngaard, J. C., Izumi, Y. and Bradley, E. F. (1971) Flux-profile relationships in the atmospheric surface layer. *Journal of the atmospheric Sciences*, **28**, 181–189.

Calaf, M., Meneveau, C. and Meyers, J. (2010) Large eddy simulation study of fully developed wind-turbine array boundary layers. *Physics of fluids*, **22**, 015110.

Carl, D. M., Tarbell, T. C. and Panofsky, H. A. (1973) Profiles of wind and temperature from towers over homogeneous terrain. *Journal of the Atmospheric Sciences*, **30**, 788–794.

Cava, D., Mortarini, L., Giostra, U., Acevedo, O. and Katul, G. (2019) Submeso motions and intermittent turbulence across a nocturnal low-level jet: A self-organized criticality analogy. *Boundary-Layer Meteorology*, 1–27.

Clarke, R. and Hess, G. (1974) Geostrophic departure and the functions a and b of rossby-number similarity theory. *Boundary-Layer Meteorology*, **7**, 267–287.

Coleman, G. (1999) Similarity statistics from a direct numerical simulation of the neutrally stratified planetary boundary layer. *Journal of the Atmospheric Sciences*, **56**, 891–900.

Coleman, G. N., Ferziger, J. and Spalart, P. (1990) A numerical study of the turbulent Ekman layer. *Journal of Fluid Mechanics*, **213**, 313–348.

Draxl, C., Hahmann, A. N., Peña, A. and Giebel, G. (2014) Evaluating winds and vertical wind shear from weather research and forecasting model forecasts using seven planetary boundary layer schemes. *Wind Energy*, **17**, 39–55.

Ekman, V. (1905) On the influence of the earth's rotation on ocean currents. *Arkiv Matematik. Astronomi och Fysil*, **2**, 1–53.

Fiedler, F. and Panofsky, H. (1972) The geostrophic drag coefficient and the 'effective'roughness length. *Quarterly Journal of the Royal Meteorological Society*, **98**, 213–220.

Floors, R., Peña, A. and Gryning, S.-E. (2015) The effect of baroclinicity on the wind in the planetary boundary layer. *Quarterly Journal of the Royal Meteorological Society*, **141**, 619–630.

Floors, R., Vincent, C. L., Gryning, S.-E., Peña, A. and Batchvarova, E. (2013) The wind profile in the coastal boundary layer: Wind lidar measurements and numerical modelling. *Boundary-layer meteorology*, **147**, 469–491.

Garratt, J. R. (1994) The atmospheric boundary layer. *Earth-Science Reviews*, **37**, 89–134.

Geernaert, G. (1988) Measurements of the angle between the wind vector and wind stress vector in the surface layer over the north sea. *Journal of Geophysical Research: Oceans*, **93**, 8215–8220.

George, W. K. and Castillo, L. (1997) Zero-pressure-gradient turbulent boundary layer. *Applied Mechanics Reviews*, **50**, 689–729.

Ghannam, K., Duman, T., Salesky, S. T., Chamecki, M. and Katul, G. (2017) The non-local character of turbulence asymmetry in the convective atmospheric boundary layer. *Quarterly Journal of the Royal Meteorological Society*, **143**, 494–507.

Ghannam, K., Katul, G. G., Bou-Zeid, E., Gerken, T. and Chamecki, M. (2018) Scaling and similarity of the anisotropic coherent eddies in near-surface atmospheric turbulence. *Journal of the Atmospheric Sciences*, **75**, 943–964.

Gryning, S.-E., Batchvarova, E., Brümmer, B., Jørgensen, H. and Larsen, S. (2007) On the extension of the wind profile over homogeneous terrain beyond the surface boundary layer. *Boundary-Layer Meteorology*, **124**, 251–268.

Gualtieri, G. and Secci, S. (2012) Methods to extrapolate wind resource to the turbine hub height based on power law: A 1-h wind speed vs. weibull distribution extrapolation comparison. *Renewable Energy*, **43**, 183–200.

Haugen, D., Kaimal, J. and Bradley, E. (1971) An experimental study of reynolds stress and heat flux in the atmospheric surface layer. *Quarterly Journal of the Royal Meteorological Society*, **97**, 168–180.

Hess, G. (1973) On rossby-number similarity theory for a baroclinic planetary boundary layer. *Journal of the Atmospheric Sciences*, **30**, 1722–1723.

Hess, G. and Garratt, J. (2002) Evaluating models of the neutral, barotropic planetary boundary layer using integral measures: Part I. overview. *Boundary-layer meteorology*, **104**, 333–358.

Högström, U. (1996) Review of some basic characteristics of the atmospheric surface layer. *Boundary-Layer Meteorology*, **78**, 215–246.

Holtslag, M., Bierbooms, W. and van Bussel, G. (2017) Extending the diabatic surface layer wind shear profile for offshore wind energy. *Renewable energy*, **101**, 96–110.

Horiguchi, M., Hayashi, T., Adachi, A. and Onogi, S. (2012) Large-scale turbulence structures and their contributions to the momentum flux and turbulence in the near-neutral atmospheric boundary layer observed from a 213-m tall meteorological tower. *Boundary-layer meteorology*, **144**, 179–198.

Jiang, Q., Wang, S. and Sullivan, P. (2018) Large-eddy simulation study of log laws in a neutral ekman boundary layer. *Journal of the Atmospheric Sciences*, **75**, 1873–1889.

Kaimal, J. and Wyngaard, J. (1990) The Kansas and Minnesota experiments. *Boundary-Layer Meteorology*, **50**, 31–47.

Katul, G. G., Porporato, A., Manes, C. and Meneveau, C. (2013) Co-spectrum and mean velocity in turbulent boundary layers. *Physics of Fluids*, **25**, 091702.

Kawai, S. and Larsson, J. (2012) Wall-modeling in large eddy simulation: Length scales, grid resolution, and accuracy. *Physics of Fluids*, **24**, 015105.

Kent, C. W., Grimmond, C. S. B., Gatey, D. and Barlow, J. F. (2018) Assessing methods to extrapolate the vertical wind-speed profile from surface observations in a city centre during strong winds. *Journal of Wind Engineering and Industrial Aerodynamics*, **173**, 100–111.

Klewicki, J. and Oberlack, M. (2015) Finite reynolds number properties of a turbulent channel flow similarity solution. *Physics of Fluids*, **27**, 095110.

Kumar, V., Kleissl, J., Meneveau, C. and Parlange, M. B. (2006) Large-eddy simulation of a diurnal cycle of the atmospheric boundary layer: Atmospheric stability and scaling issues. *Water Resources Research*, **42**.

Marusic, I., Monty, J. P., Hultmark, M. and Smits, A. J. (2013) On the logarithmic region in wall turbulence. *Journal of Fluid Mechanics*, **716**.

Mason, P. J. and Thomson, D. J. (1992) Stochastic backscatter in large-eddy simulations of boundary layers. *Journal of Fluid Mechanics*, **242**, 51–78.

Meneveau, C. and Marusic, I. (2013) Generalized logarithmic law for high-order moments in turbulent boundary layers. *Journal of Fluid Mechanics*, **719**.

Mirocha, J. D., Churchfield, M. J., Muñoz-Esparza, D., Rai, R. K., Feng, Y., Kosović, B., Haupt, S. E., Brown, B., Ennis, B. L., Draxl, C. et al. (2018) Large-eddy simulation sensitivities to variations of configuration and forcing parameters in canonical boundary-layer flows for wind energy applications. *Wind Energy Science*, **3**, 589–613.

Momen, M. and Bou-Zeid, E. (2016) Large-eddy simulations and damped-oscillator models of the unsteady ekman boundary layer. *Journal of the Atmospheric Sciences*, **73**, 25–40.

Momen, M., Bou-Zeid, E., Parlange, M. B. and Giometto, M. (2018) Modulation of mean wind and turbulence in the atmospheric boundary layer by baroclinicity. *Journal of the Atmospheric Sciences*, **75**, 3797–3821.

Monin, A. S. and Obukhov, A. M. (1954) Basic laws of turbulent mixing in the surface layer of the atmosphere. *Contrib. Geophys. Inst. Acad. Sci. USSR*, **151**, 163–187.

Murthy, K. and Rahi, O. (2017) A comprehensive review of wind resource assessment. *Renewable and Sustainable Energy Reviews*, **72**, 1320–1342.

Nieuwstadt, F. (1983) On the solution of the stationary, baroclinic Ekman-layer equations with a finite boundary-layer height. *Boundary-Layer Meteorology*, **26**, 377–390.

O'Brien, J. J. (1970) A note on the vertical structure of the eddy exchange coefficient in the planetary boundary layer. *Journal of the Atmospheric Sciences*, **27**, 1213–1215.

Pan, Y. and Patton, E. G. (2017) On determining stationary periods within time series. *Journal of Atmospheric and Oceanic Technology*, **34**, 2213–2232.

Peña, A., Floors, R., Sathe, A., Gryning, S.-E., Wagner, R., Courtney, M. S., Larsén, X. G., Hahmann, A. N. and Hasager, C. B. (2016) Ten years of boundary-layer and wind-power meteorology at høvsøre, denmark. *Boundary-Layer Meteorology*, **158**, 1–26.

Peña, A., Gryning, S.-E. and Mann, J. (2010) On the length-scale of the wind profile. *Quarterly Journal of the Royal Meteorological Society*, **136**, 2119–2131.

Rossby, C.-G. and Montgomery, R. B. (1935) *The layer of frictional influence in wind and ocean currents*, vol. 3. Massachusetts Institute of Technology and Woods Hole Oceanographic Institution.

Salesky, S. T., Katul, G. G. and Chamecki, M. (2013) Buoyancy effects on the integral lengthscales and mean velocity profile in atmospheric surface layer flows. *Physics of Fluids*, **25**, 105101.

Simiu, E., Shi, L. and Yeo, D. (2016) Planetary boundary-layer modelling and tall building design. *Boundary-layer meteorology*, **159**, 173–181.

Sorbjan, Z. (2004) Large-eddy simulations of the baroclinic mixed layer. *Boundary-layer meteorology*, **112**, 57–80.

Spalart, P. R., Coleman, G. N. and Johnstone, R. (2008) Direct numerical simulation of the ekman layer: a step in reynolds number, and cautious support for a log law with a shifted origin. *Physics of Fluids*, **20**, 101507.

Stoll, R. and Porté-Agel, F. (2006) Effect of roughness on surface boundary conditions for large-eddy simulation. *Boundary-Layer Meteorology*, **118**, 169–187.

Stull, R. B. (1988) *An Introduction to Boundary Layer Meteorology*. Klumer academic, Dordrecht.

Svensson, G. and Holtslag, A. A. (2009) Analysis of model results for the turning of the wind and related momentum fluxes in the stable boundary layer. *Boundary-layer meteorology*, **132**, 261–277.

Tennekes, H. (1973) The logarithmic wind profile. *Journal of the Atmospheric Sciences*, **30**, 234–238.

Tennekes, H., Lumley, J. L., Lumley, J. et al. (1972) *A first course in turbulence*. MIT press.

Townsend, A. (1961) Equilibrium layers and wall turbulence. *Journal of Fluid Mechanics*, **11**, 97–120.

Wallace, J. M. and Hobbs, P. V. (2006) *Atmospheric science: an introductory survey*, vol. 92. Elsevier.

Wu, J. (1980) Wind-stress coefficients over sea surface near neutral conditions—a revisit. *Journal of Physical Oceanography*, **10**, 727–740.

Wu, X. and Moin, P. (2009) Direct numerical simulation of turbulence in a nominally zero-pressure-gradient flat-plate boundary layer. *Journal of Fluid Mechanics*, **630**, 5–41.

Yang, B., Qian, Y., Berg, L. K., Ma, P.-L., Wharton, S., Bulaevskaya, V., Yan, H., Hou, Z. and Shaw, W. J. (2017) Sensitivity of turbine-height wind speeds to parameters in planetary boundary-layer and surface-layer schemes in the weather research and forecasting model. *Boundary-layer meteorology*, **162**, 117–142.

Zilitinkevich, S. and Esau, I. (2002) On integral measures of the neutral barotropic planetary boundary layer. *Boundary-layer meteorology*, **104**, 371–379.

Zilitinkevich, S. S. (1972) On the determination of the height of the Ekman boundary layer. *Boundary-Layer Meteorology*, **3**, 141–145.

— (1989) Velocity profiles, the resistance law and the dissipation rate of mean flow kinetic energy in a neutrally and stably stratified planetary boundary layer. *Boundary-Layer Meteorology*, **46**, 367–387.

Zilitinkevich, S. S. and Esau, I. N. (2003) The effect of baroclinicity on the equilibrium depth of neutral and stable planetary boundary layers. *Quarterly Journal of the Royal Meteorological Society*, **129**, 3339–3356.

— (2005) Resistance and heat-transfer laws for stable and neutral planetary boundary layers: Old theory advanced and re-evaluated. *Quarterly Journal of the Royal Meteorological Society*, **131**, 1863–1892.

TABLE 1 Imposed and derived LES parameters for the barotropic ABL. z_0 = 0.1 m in all these cases.

Simulation name	Ro ($\times 10^5$)	G_0 (m s^{-1})	u_* (m s^{-1})	f ($\times 10^{-4}$s^{-1})	u_*/f (m)	α_0 (deg)	B	c
B1	2.9	4	0.16	1.4	1168	18	2.4	3.6
B2	4.3	6	0.24	1.4	1680	17	2.5	3.5
B3	5.8	6	0.24	1.03	2200	16	2.6	3.5
B4	8.2	6	0.22	0.73	3027	15	2.6	3.5
B5	15.9	6	0.22	0.38	5850	16	2.6	3.3

TABLE 2 Imposed and derived LES parameters for the baroclinic ABL. The external parameters in all these cases are based on the barotropic simulation B2 in Table 1 (reproduced here as simulation Barotropic for comparison). The height δ = 1000 m is used in all these simulations. Positive and negative shear cases are denoted by S^+ and S^-, warm and cold advection by A^+ and A^-, and a combination case (mixed advection) by S^-A^-. The diagnostic values of c (7th column) and B^{diag} are obtained from LES output. Prognostic values B^{prog} are modelled after Equation 23b using the mean fitted value c = 2.7 from Figure 3b.

Simulation name	$\frac{U_T}{\delta}$ ($\times 10^{-3} s^{-1}$)	$\frac{V_T}{\delta}$ ($\times 10^{-3} s^{-1}$)	β_0 (deg)	u_* (m s^{-1})	α_0 (deg)	c	B^{diag}	B^{prog}
Barotropic	0	0	0	0.24	17	3.5	2.5	2.5
S^+	+6	0	0	0.37	1	3	0.5	0.65
S^-	-6	0	180	0.15	45	2.2	9.7	8.4
A^-	0	+6	90	0.3	30	2.5	4.5	4.1
A^+	0	-6	-90	0.26	-30	3.1	-4.8	-3.6
S^-A^-	-4.2	+4.2	135	0.25	50	2.5	6.7	6.5

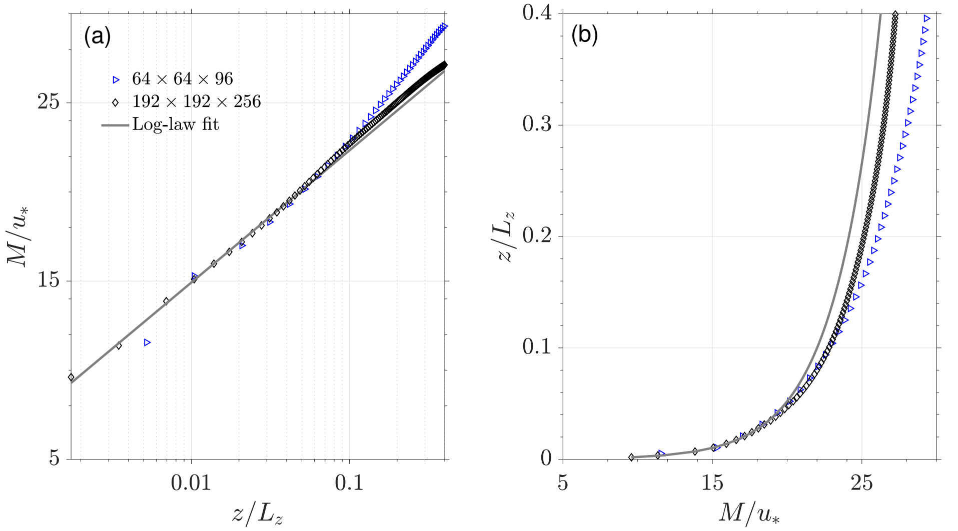

FIGURE 1 Logarithmic profile fits to the normalized mean velocity in channel flow (No-Coriolis cases) at different LES grid resolutions. (a) Log-linear plot up to $0.4L_z$ with L_z = 1500 m; and (b) the corresponding linear-linear profiles. The solid grey is the logarithmic fit resulting in κ =0.387 and z_0 =0.1.

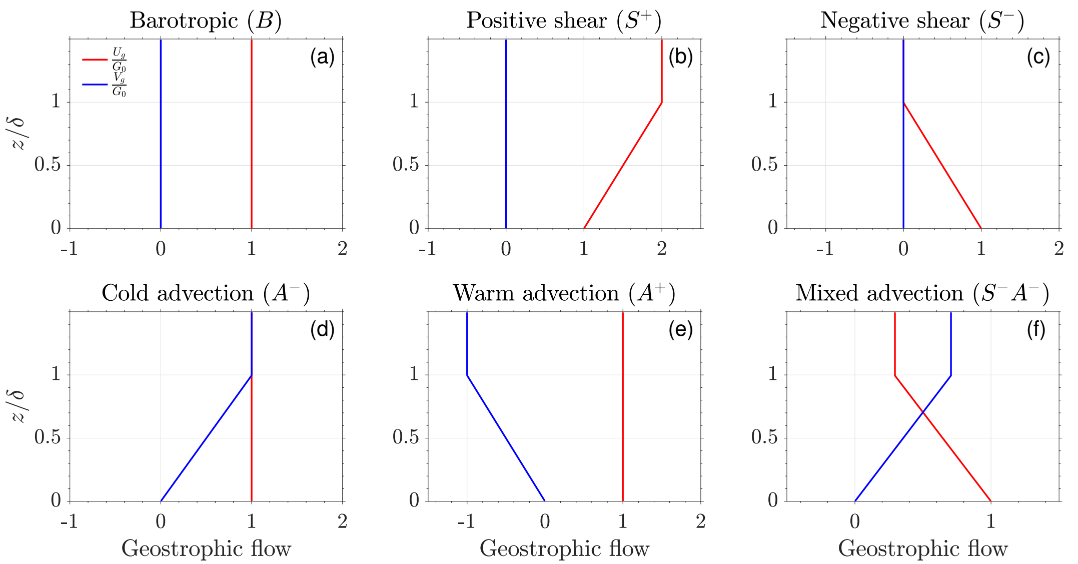

FIGURE 2 Geostrophic wind profiles normalized by G_0 for the barotropic and baroclinic cases. The magnitude of the geostrophic wind vector is $G(z) = \sqrt{U_g^2 + V_g^2}$.

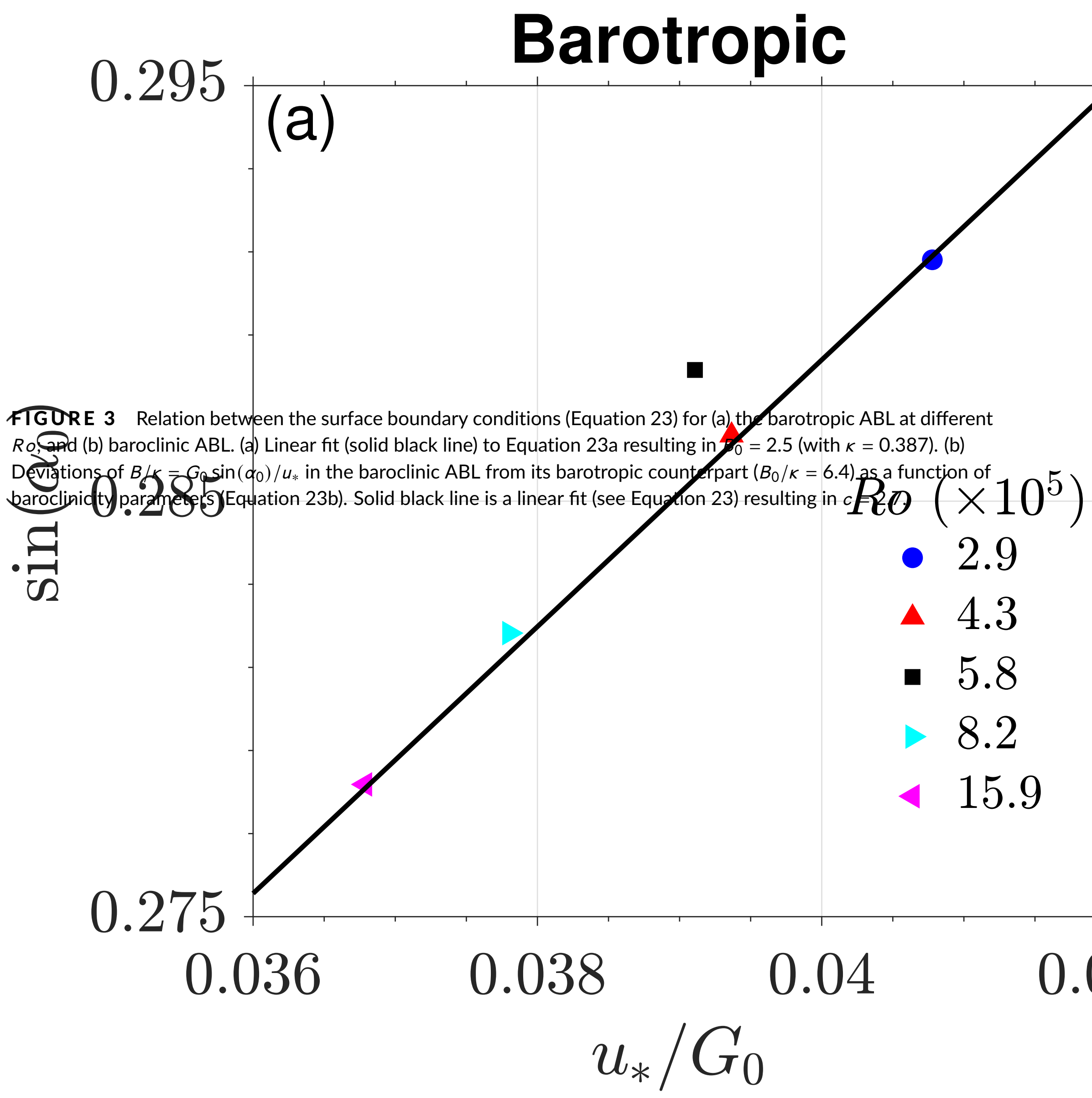

FIGURE 3 Relation between the surface boundary conditions (Equation 23) for (a) the barotropic ABL at different Ro, and (b) baroclinic ABL. (a) Linear fit (solid black line) to Equation 23a resulting in B_0 = 2.5 (with κ = 0.387). (b) Deviations of $B/\kappa = G_0 \sin(\alpha_0)/u_*$ in the baroclinic ABL from its barotropic counterpart (B_0/κ = 6.4) as a function of baroclinicity parameters (Equation 23b). Solid black line is a linear fit (see Equation 23) resulting in c = 2.7.

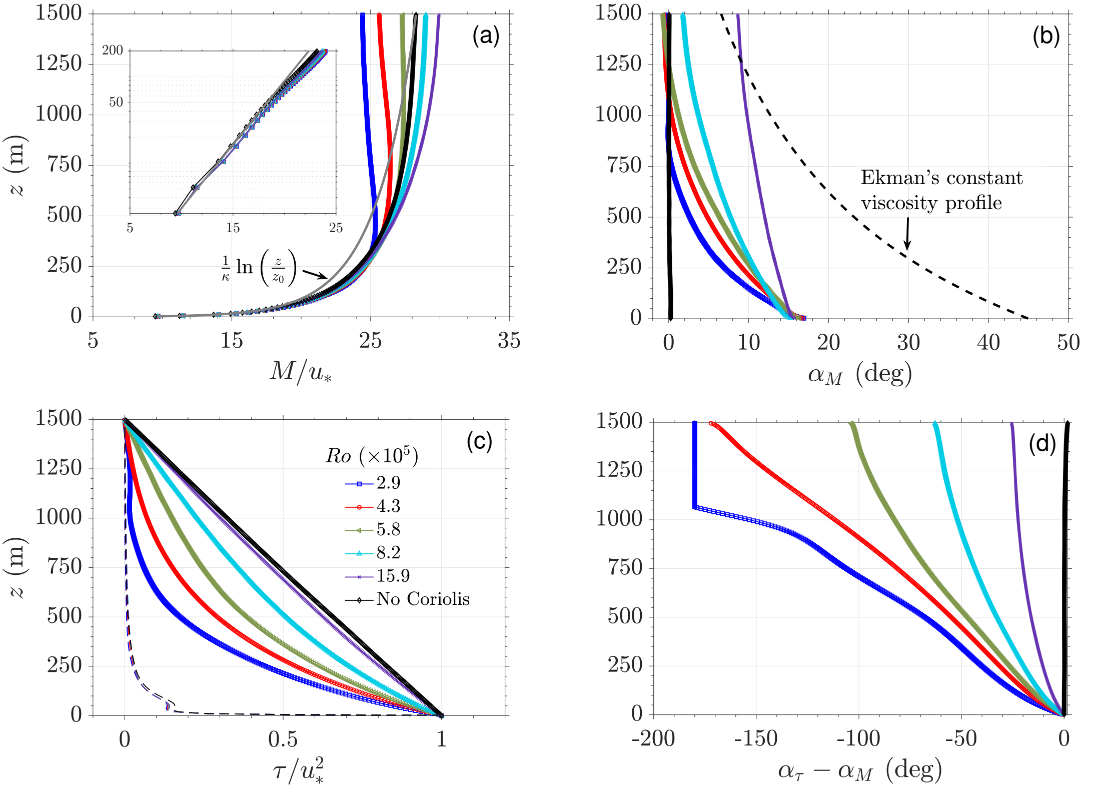

FIGURE 4 LES profiles for the barotropic ABL at different Rossby number (Ro) along with the No-Coriolis simulation. Upper panel shows (a) mean wind profiles $M = \sqrt{\overline{U}^2 + \overline{V}^2}$ normalized by u_*. The log-law with $\kappa = 0.387$ is also shown in grey (color online). The inset is a blow-up of the lowest 200 m of the domain; and (b) Cross-isobaric angle α_M along with Ekman's exponential solution (dashed line). Lower panel shows (c) the magnitude of the total (resolved + SGS) stress $\tau = \sqrt{\tau_x^2 + \tau_y^2}$ normalized by u_*^2 with the SGS stresses shown as thin dashed lines; and (d) difference between the angles of the stress and wind vectors $\alpha_\tau - \alpha_M$. The kink in the upper part ($z > 1000$ m) of the profile of $\alpha_\tau - \alpha_M$ for $Ro = 2.9 \times 10^5$ (blue line in panel (d)) is imposed: since both stress components become negligibly small above this height we set the angle difference to 180° (the value at $z \approx 1000$ m).

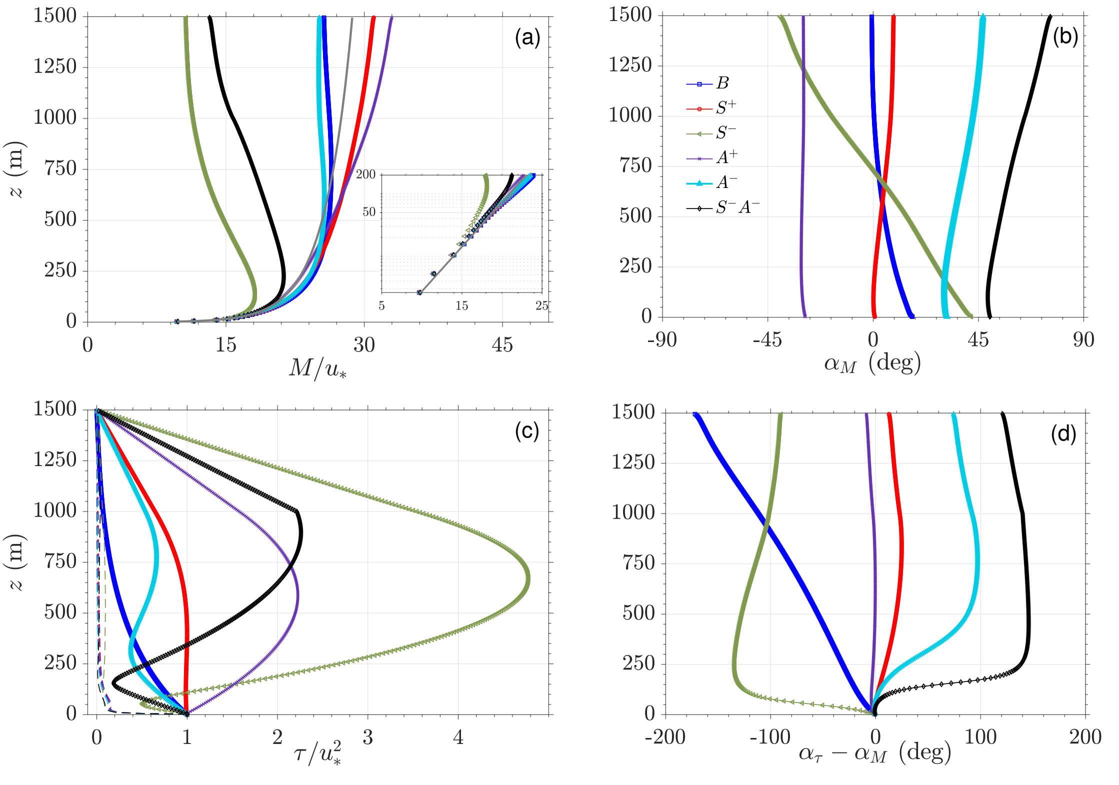

FIGURE 5 LES profiles for the baroclinic ABL with different orientation of the geostrophic wind vector (see Table 2 for simulation names). A barotropic simulation (shown as B in the legend) is also reproduced for reference. (a) mean wind profiles normalized by u_*. The log-law with κ =0.387 is also shown in grey (color online) and the inset is a blow-up of the lowest 200 m of the domain; and (b) Wind angle α_M relative to surface geostrophic wind. Lower panel shows (c) the magnitude of the total (resolved + SGS) stress normalized by u_*^2 with the SGS stresses shown as thin dashed lines; and (d) difference between the angles of the stress and wind vectors $\alpha_\tau - \alpha_M$.

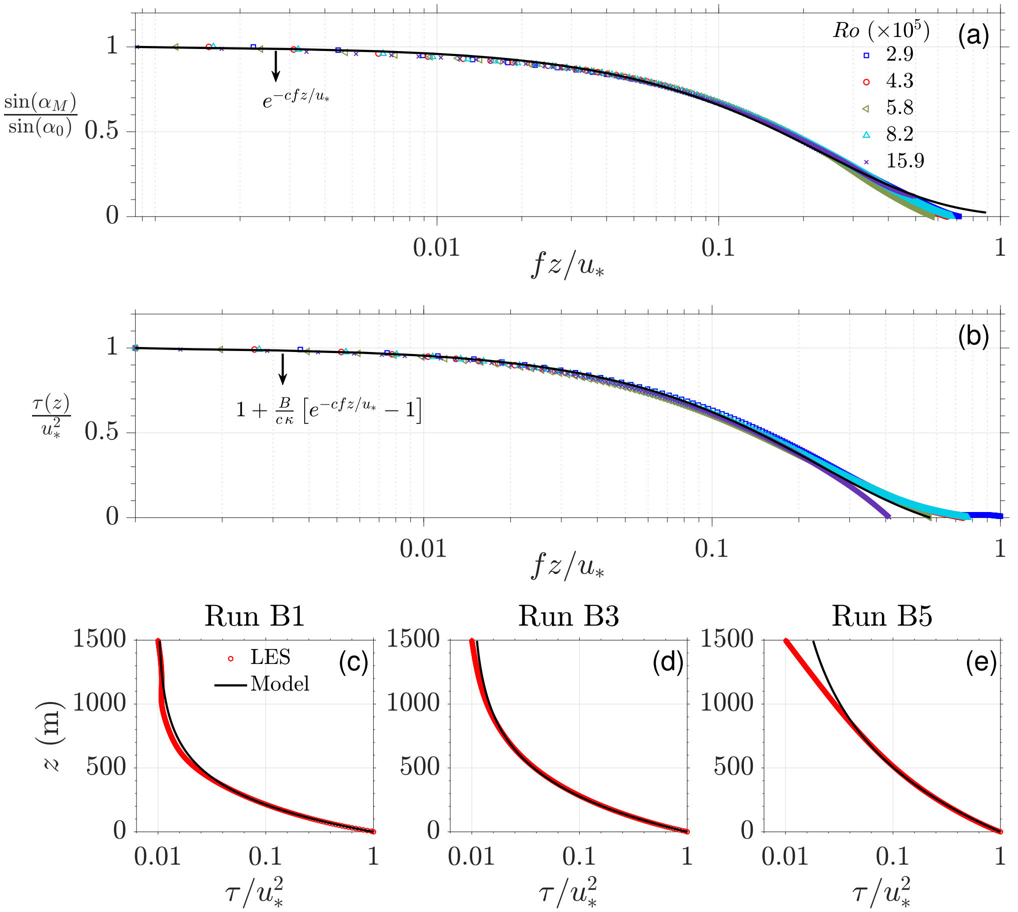

FIGURE 6 Model validation for the cross-isobaric angle α_M and the stress profiles in the barotropic ABL. (a) and (b) show the profiles of $\sin(\alpha_M)$ and $\tau(z)$ (magnitude of the resolved+SGS stress) normalized by their surface values. Symbols are LES output and solid black lines represent the models in Equations 24 and 25b both with $\gamma = 0$, $c = 3.5$, $B = 2.5$, and $\kappa = 0.387$. Individual examples for simulations B1, B3, and B5 are shown in (c), (d), and (e), respectively.

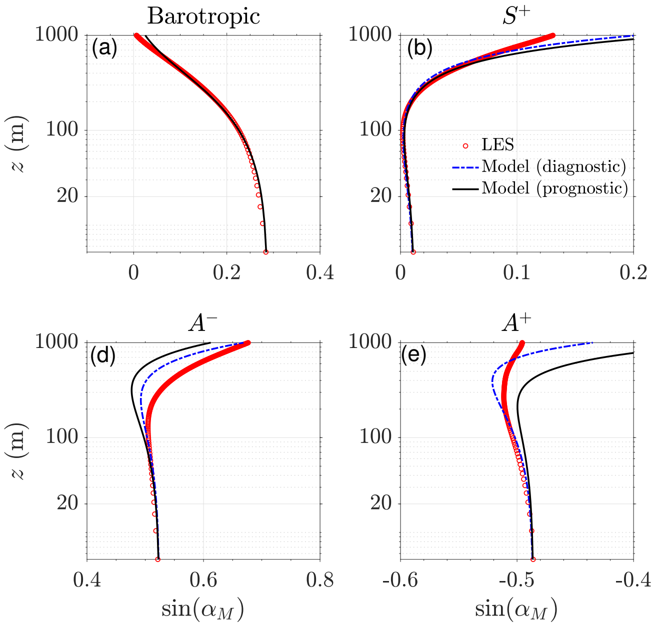

FIGURE 7 Model for $\sin(\alpha_M)$ in the baroclinic ABL. The height z is on log-scale. Symbols are LES output, dashed (blue) and solid (black) lines represent, respectively, the diagnostic model (Equation 24 with the parameters c and B^{diag} from Table 2), and prognostic model (Equation 24 with the parameters $c = 2.7$ and B^{prog} from Table 2).

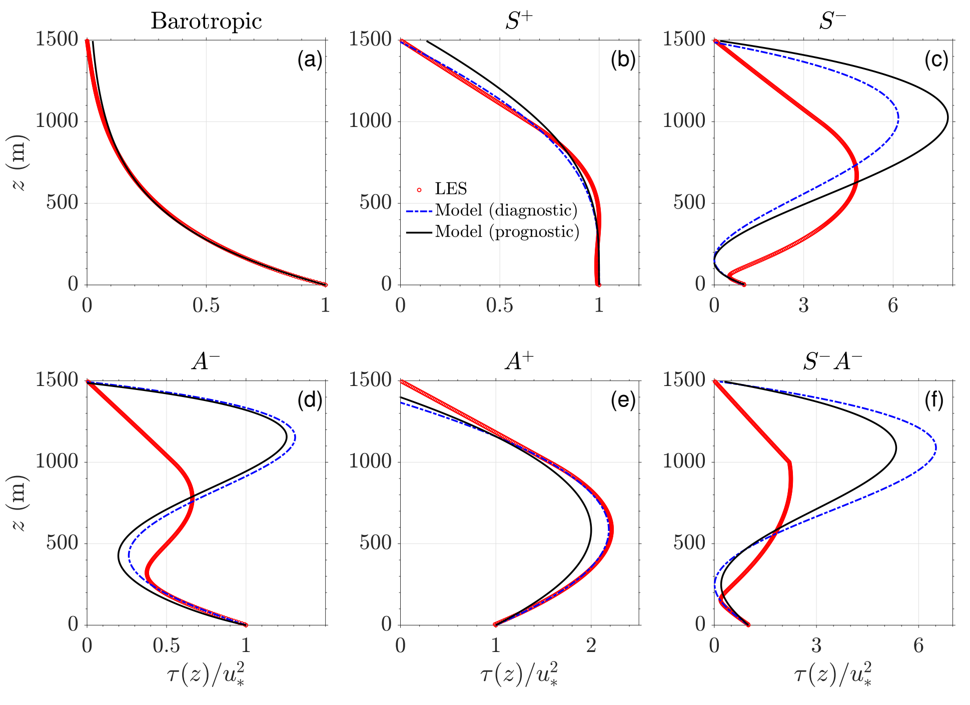

FIGURE 8 Performance of the stress model (Equation 25a) in the baroclinic ABL. Table 2 lists the parameters B and c used in the diagnostic and prognostic models as described in the main text and in Figure 7.

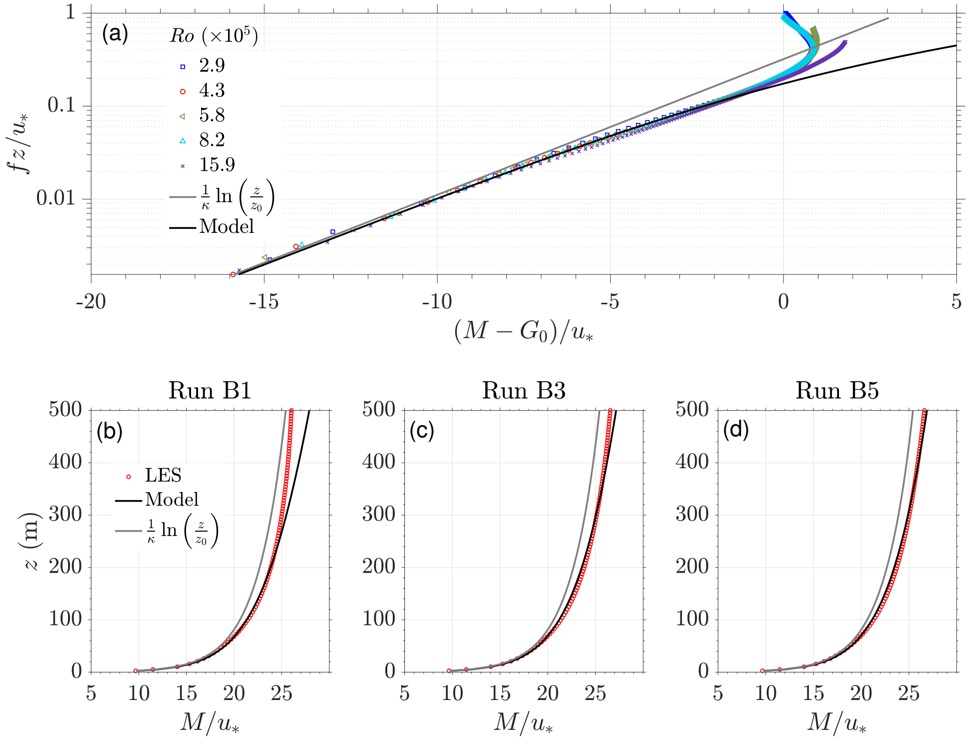

FIGURE 9 Comparison between the wind model (Equation 29 with $\gamma = 0$, $B = 2.5$, and $c = 3.5$) and the logarithmic scaling for the barotropic ABL at different Ro. (a) Linear-log wind-defect (ageostrophic) profile, and [(b), (c), and (d)] are individual examples of the wind profile in the lowest 500 m of the ABL. Symbols are LES output and grey and black solid lines are the log-law and the model, respectively.

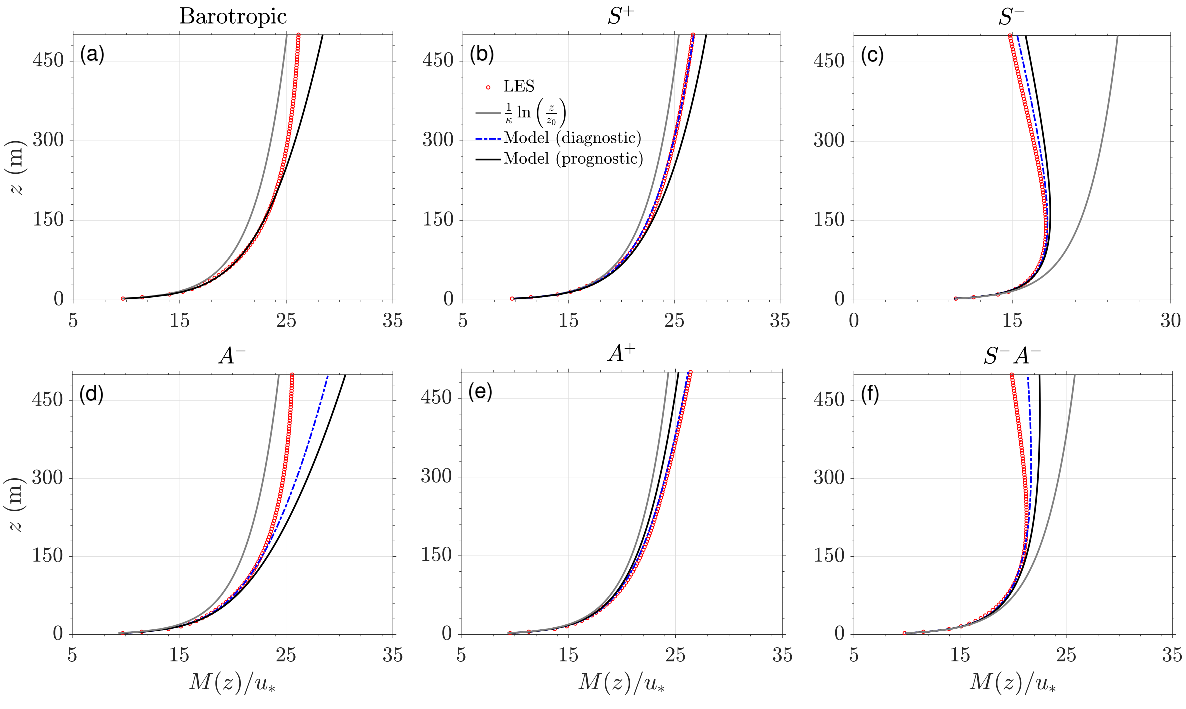

FIGURE 10 Comparison between the wind model (Equation 29) and the logarithmic scaling for the baroclinic ABL in the lowest 500 m of the domain. The parameters B and c used in Equation 29 are the same as those used for the stress profiles (Figure 8) and reported in Table 2.

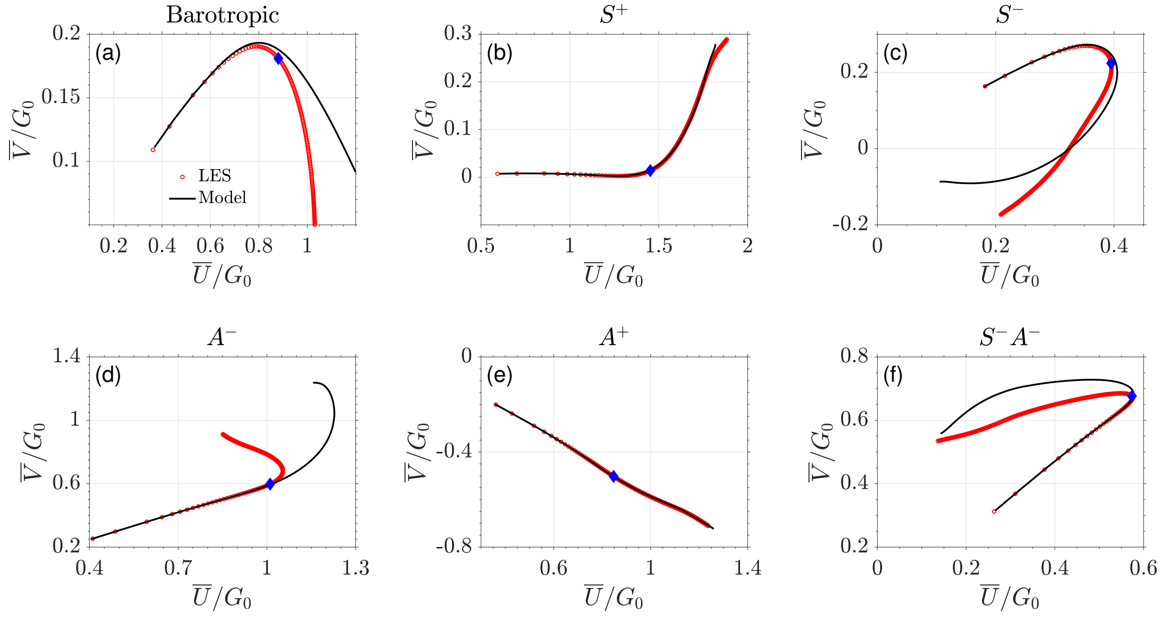

FIGURE 11 Model performance for the component winds, $\overline{U} = M\cos(\alpha_M)$ and $\overline{V} = M\sin(\alpha_M)$, shown as an Ekman spiral and normalized by the surface geostrophic wind G_0. Symbols represent LES output and solid black lines are the model with wind speed M obtained from Equation 29 and wind angle $\sin(\alpha_M)$ from Equation 24. The solid diamond symbol indicates a height of 200 m above the surface. The parameters B^{diag} and c from Table 2 are used in Equations 24 and 29.